INTERNATIONAL JOURNAL OF ADAPTIVE CONTROL AND SIGNAL PROCESSING
Int. J. Adapt. Control Signal Process. 2015; **??**:1–23
Published online in Wiley InterScience (www.interscience.wiley.com). DOI: 10.1002/10.1002/acs

Design of Inertial Navigation Systems for Marine Craft with Adaptive Wave Filtering aided by Triple-Redundant Sensor Packages

Torleiv Håland Bryne*, Thor I. Fossen and Tor A. Johansen

Centre for Autonomous Marine Operations and Systems (AMOS), Department of Engineering Cybernetics, Norwegian University of Science and Technology, NO-7491 Trondheim, Norway.

SUMMARY

Marine craft feedback control systems typically require estimates of position, velocity and heading where the wave-induced motions should be suppressed. This paper presents a strapdown inertial navigation system with adaptive wave filtering. Wave filtering based on inertial navigation systems differ from previous vessel-model-based designs which require knowledge of vessel parameters and mathematical models for estimation of thruster and wind forces and moments based on auxiliary sensors. The origin of the inertial navigation system error states is proven to be uniformly semiglobally exponentially stable (USGES). The wave-filtering scheme uses the estimated states of the inertial navigation system to separate the low-frequency motion of the craft from the wave-frequency motions. The observer structure also allows for estimation of the time-varying encounter frequency by using a signal-based frequency tracker or an adaptive observer. Finally, the structural properties of the triple-redundant sensors packages have been utilized to obtain optimal and robust sensor fusion with respect to sensor performance and faults. Copyright © 2015 John Wiley & Sons, Ltd.

Received ...

KEY WORDS: Dynamic Positioning; Inertial Navigation; Adaptive Wave Filter; Marine Systems; Sensor Redundancy

1. INTRODUCTION

Wave filtering is a vital part of dynamic positioning (DP) and marine autopilot systems. This is applied such that only the low-frequency (LF) components of the vessel's surge, sway and heading motions are considered by the control system. Fossen [1, Ch. 11, p. 286] states: *Wave filtering can be defined as the reconstruction of the low-frequency motion components from noisy measurements of position, heading and in some cases velocity and acceleration by means of a state observer or a filter.* Wave-induced craft motion, also known as the wave-frequency (WF) motion, oscillates about the vessel's LF motion as seen in Figure 1. By preventing the WF motion to enter the control loop, only the mean-vessel motion is considered by the controller which will result in less fluctuations of thrust. Hence, from a practical point of view, wave filtering has the potential to reduce wear of mechanical equipment, such as thrusters and engines, together with reducing the fuel consumption and emissions from the vessel's engines.

*Correspondence to: Torleiv H. Bryne, Centre for Autonomous Marine Operations and Systems (AMOS), Department of Engineering Cybernetics, Norwegian University of Science and Technology, NO-7491 Trondheim, Norway. E-mail: torleiv.h.bryne@itk.ntnu.no.

Contract/grant sponsor: The Research Council of Norway and Rolls-Royce Marine through the Centres of Excellence funding scheme and the MAROFF programme; contract/grant number: 223254 and 225259, respectively.

Copyright © 2015 John Wiley & Sons, Ltd.
Prepared using acsauth.cls *[Version: 2010/03/27 v2.00]*

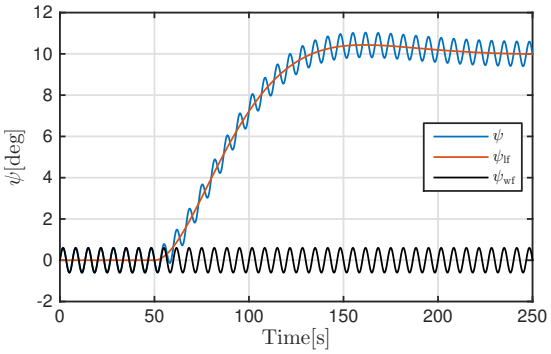

Figure 1. Illustration of the total (blue), LF (red) and WF (black) motion of the vessel's heading, ψ.

Observer-based wave filtering was first introduced by Balchen et al. [2] and later extended by Sælid et al. [3] utilizing the vessel model and the Extended Kalman Filter (EKF) algorithm. This wave-filtering technique makes use of the knowledge of the encounter frequency of the waves, that is the peak frequency of the wave spectra shifted due to the speed of the vessel, to separate the LF and WF motion. See, Fossen [1, Ch. 8.2.3, pp. 210–211] for details. Fossen and Perez [4] presented an overview of Kalman filter (KF) and model-based techniques for wave filtering in DP and autopilot designs. One potential shortcoming of the EKF is that global stability and robustness properties are nontrivial to prove.

Another model-based design followed with Vik and Fossen [5], which developed an uniformly semiglobal exponential stable observer (USGES) including wave filtering. Lauvdal and Fossen [6] presented an autopilot design with an adaptive controller in cascade with a notch filter where the latter performed the wave filtering. Furthermore, Fossen and Strand [7] developed an nonlinear globally exponentially stable (GES) observer, with wave filtering of horizontal position and heading measurements. The passivity result of [7] is valid for constant encounter frequency. Later Strand and Fossen [8] extended their work to include online estimation of the encounter frequency. Torsetnes et al. [9] handled time-varying encounter frequencies with a globally contracting observer employing gain-scheduling. Nguyen et al. [10] and Brodtkorb et al. [11] dealt with time-varying encounter frequencies utilizing four passive observers, based on [7], parametrized with four different and constant encounter frequencies employed in a hybrid framework.

Hassani et al. [12] presented an adaptive wave filtering scheme utilizing the Kalman filter and a linearized vessel model, yielding a local result, where the encounter frequency candidates had to be chosen in advance. Later, these results were extended by Hassani et al. [13]–[14] to include estimation of the dominating wave frequency with a discrete-time gradient based algorithm and with a maximum likelihood algorithm together with a bank of Kalman filters, respectively.

Bryne et al. [15] have developed a six degree of freedom (DOF), time-varying nonlinear inertial navigation system (INS) observer, with USGES stability properties, exploiting the position reference system's quality indicator, customized for marine surface vessels, based on the results of Grip et al. [16]. However, Bryne et al. did not consider wave filtering. Results related to inertial sensor-based wave filtering of both position and heading, in part except from Lindegaard and Fossen [17] which utilized acceleration measurements in a model-based regime, is a gap in the literature.

A radically different approach with a wave-filtering effect is provided in Veksler et al. [18]. By allowing a dynamics window in the thrust allocation system, the thrust variation due to the wave-induced motion, and other high-frequency consumer power variations, is reduced. This leads to less wear on machinery, as well as reduced emission and fuel consumption from the vessel's engines.

1.1. Main Contribution of the Paper

This paper addresses a similar problem as the nonlinear adaptive wave filter of Strand and Fossen [8]. The wave-filtering design to be presented is based upon inertial sensors and an INS, as opposed to exploiting the vessel model and auxiliary sensors together with mathematical models to obtain thruster and wind generated forces and moments. The main contributions are:

Copyright © 2015 John Wiley & Sons, Ltd.
Prepared using acsauth.cls

DOI: 10.1002/10.1002/acs

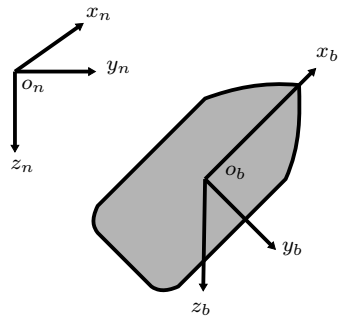

Figure 2. Definitions of the BODY and NED reference frames, denoted {b} and {n}, respectively.

- Development of a vessel-model-free INS with wave filtering. The design incorporates an exogenous time-varying encounter frequency, $\omega_e(t)$, which can be estimated using an adaptive signal processing based algorithm, e.g. Belleter et al. [19].
- Signal processing to monitor the triple-redundant sensor packages for errors and faults, including single fault estimation, and to perform online tuning of the observers.

2. KINEMATICS AND WAVE-FILTER MODELING

2.1. *Reference Frames*

This paper employs two reference frames, North, East, Down (NED) and BODY, denoted $\{n\}$ and $\{b\}$, respectively as seen in Fig. 2. NED is a local Earth-fixed frame, while the BODY frame is fixed to the vessel. The origin of {b} is defined at the nominal center of gravity of the vessel. The x-axis is directed from aft to fore, the y-axis is directed to starboard and the z-axis points downwards.

2.2. *Kinematic Strapdown Equations*

Let the NED position and linear velocity be expressed as $\boldsymbol{p}^n = [p_x,\, p_y,\, p_z]^\intercal$ and $\boldsymbol{v}^n = [v_x,\, v_y,\, v_z]^\intercal$, respectively, while the specific force of the vessel is denoted $\boldsymbol{f}^b \in \mathbb{R}^3$. The local gravity vector is denoted $\boldsymbol{g}^n$. Moreover, the attitude of the craft is represented by an unit quaternion $\boldsymbol{q}_b^n$ characterizing the rotation from BODY to the NED frame. The unit quaternion is defined as $\boldsymbol{q}_b^n := [s,\, \boldsymbol{r}^\intercal]^\intercal$ where $s \in \mathbb{R}^1$ denotes the real part whereas, $\boldsymbol{r} \in \mathbb{R}^3$ constitutes the vector part and is given as $\boldsymbol{r} = [r_1,\, r_2,\, r_3]^\intercal$. The conjugate of a given $\boldsymbol{q} = \boldsymbol{q}_b^n$ is denoted $\boldsymbol{q}^*$ and is given as $\boldsymbol{q}^* = [s,\, -\boldsymbol{r}^\intercal]^\intercal$. Moreover, $\|\boldsymbol{q}\| = 1$, where $\|\cdot\|$ denotes the Euclidean norm. From, $\boldsymbol{q}_b^n$, the rotation matrix $\boldsymbol{R}_b^n \in SO(3)$ can be calculated according to $\boldsymbol{R}(\boldsymbol{q}_b^n) = \boldsymbol{I}_3 + 2s\boldsymbol{S}(\boldsymbol{r}) + 2\boldsymbol{S}(\boldsymbol{r})^2$, as in e.g. [16], where $\boldsymbol{I}_3$ is the 3×3 identity matrix, while $\boldsymbol{S}(\cdot)$ denotes the skew-symmetric matrix and is given such that $\boldsymbol{v}_1 \times \boldsymbol{v}_2 = \boldsymbol{S}(\boldsymbol{v}_1)\boldsymbol{v}_2$ for two given vectors $\boldsymbol{v}_1, \boldsymbol{v}_2 \in \mathbb{R}^3$. Furthermore, the angular transformation matrix is given as $\boldsymbol{T}(\boldsymbol{q}_b^n) = [-\boldsymbol{r},\, s\boldsymbol{I}_3 + \boldsymbol{S}^\intercal(\boldsymbol{r})]^\intercal$ similar to Fossen [1, Ch.2.2.2] and references therein. Moreover, $\boldsymbol{\omega}_{b/n}^b \in \mathbb{R}^3$ is the angular velocity given in {b}. Finally, the constant biases of the three-axis rate gyro is denoted $\boldsymbol{b}_g^b \in \mathbb{R}^3$. With these preliminaries stated, the strapdown equations are given as:

$$\dot{p}_I^n = p_z^n \tag{1}$$
$$\dot{\boldsymbol{p}}^n = \boldsymbol{v}^n \tag{2}$$
$$\dot{\boldsymbol{v}}^n = \boldsymbol{R}(\boldsymbol{q}_b^n)\boldsymbol{f}^b + \boldsymbol{g}^n \tag{3}$$
$$\dot{\boldsymbol{q}}_b^n = \boldsymbol{T}(\boldsymbol{q}_b^n)\boldsymbol{\omega}_{b/n}^b \tag{4}$$
$$\dot{\boldsymbol{b}}_g^b = \boldsymbol{0}, \tag{5}$$

where (1)–(5) are obtained from Bryne et al. [15], extending the formulation in Grip et al. [16] with the integral of the vertical heave position, p_z^n, denoted p_I^n which is an auxiliary variable defined in order to utilize a virtual vertical reference (VVR) aiding measurement presented in Section 2.4.

Copyright © 2015 John Wiley & Sons, Ltd.
Prepared using acsauth.cls

DOI: 10.1002/10.1002/acs

The strapdown equations applied in this paper are suitable for marine surface vessels employing local navigation. Moreover, the $\{n\}$ frame is assumed to be nonrotating and fixed to the average sea surface level. According to Fossen [1, Ch. 2.1] this is a reasonable assumption for DP where the vessel's motion is confided to a smaller geographical region. The local gravity vector, $\boldsymbol{g}^n$, is assumed to be known. In practice this will not be completely valid, nevertheless the effect of the gravity error will be small compared to the standard deviation of the position reference systems.

2.3. Modeling of First-order Wave-induced Motion

All the sensor measurements contain both the LF and WF motions of the vessel. Therefore the estimates from a INS will contain both motion components. In order to separate the LF motion from the WF motion, linear models, exploiting the superposition principle, can be utilized to capture the main dynamics of the oscillatory wave-induced motion due to first-order wave-induced forces on the hull. The models are parameterized with the dominant wave encounter frequency, ω_e, the relative damping ratio, λ, and the gain, K_{w_i}, where the latter is a measure of the wave excitation intensity. The WF component of the i^{th} measurement can be written as $y_{\text{wf}_i} = h_{\text{wf}_i}(s)w_i$ with

$$h_{\text{wf}_i}(s) = \frac{K_{w_i} s}{s^2 + 2\lambda\omega_e s + \omega_e^2}, \tag{6}$$

as in Fossen [1, Ch. 8.2.6], where $w_i \in \mathbb{R}^n$ is assumed to be the driving noise of the WF model and being white Gaussian noise.

The wave encounter frequency is time dependent, continuous, positive, and uniformly bounded, $0 < \omega_{e,\min} \leq \omega_e(t) \leq \omega_{e,\max} < \infty$. The relative damping ratio can be considered as a known constant. Fossen [1, Ch 8.2] recommends $\lambda = 0.1$ and $\lambda = 0.26$ for the JONSWAP and the Modified Pierson–Moskowitz (MPM) spectra, respectively. Furthermore, the time variation of $\omega_e(t)$ is dealt with using a the state-space representation given by:

$$\dot{\xi}_{\text{wf}_i} = y_{\text{wf}_i} \tag{7}$$

$$\dot{y}_{\text{wf}_i} = -\omega_e^2(t)\,\xi_{\text{wf}_i} - 2\lambda\,\omega_e(t)\,y_{\text{wf}_i} + E_i w_i \tag{8}$$

where (7)–(8) is a realization of (6) with $E_i = K_{w_i}$. On the other hand, the dynamics of the LF measurement component is given as:

$$\dot{y}_{\text{lf}_i} = u_i \tag{9}$$

where u_i is a given input signal. Finally, the measurement, y_i, is given by:

$$y_i = y_{\text{lf}_i} + y_{\text{wf}_i}. \tag{10}$$

Eqs. (7)–(10) can be written in matrix form as:

$$\dot{\boldsymbol{x}}_i = \boldsymbol{A}(t)\boldsymbol{x}_i + \boldsymbol{B}u_i + \boldsymbol{E}_i w_i \tag{11}$$

$$y_i = \boldsymbol{C}\boldsymbol{x}_i \tag{12}$$

with $\boldsymbol{x}_i = [\xi_{\text{wf}_i},\, y_{\text{wf}_i},\, y_{\text{lf}_i}]^\intercal$ and

$$\boldsymbol{A}(t) = \begin{bmatrix} 0 & 1 & 0 \\ -\omega_e^2(t) & -2\lambda\omega_e(t) & 0 \\ 0 & 0 & 0 \end{bmatrix}, \quad \boldsymbol{B} = \begin{bmatrix} 0 \\ 0 \\ 1 \end{bmatrix}, \quad \boldsymbol{C} = \begin{bmatrix} 0 & 1 & 1 \end{bmatrix}, \quad \boldsymbol{E}_i = \begin{bmatrix} 0 \\ K_{w_i} \\ 0 \end{bmatrix}. \tag{13}$$

2.4. Sensor Configuration and Noise Models

The observer design is based upon a sensor configuration consisting of an IMU, a VVR together with triple-redundant position and heading reference sensor packages, respectively. The measurements are:

1. Position measurements from the triple-redundant position reference package given in the $\{n\}$ frame, $\boldsymbol{p}^n_{\text{PosRef}} = \boldsymbol{p}^n$.

Copyright © 2015 John Wiley & Sons, Ltd.
Prepared using acsauth.cls

DOI: 10.1002/10.1002/acs

2. VVR measurement: $p_I^n = 0$, for all $t \geq 0$, motivated by Godhavn [20]. The mean vertical position of the vessel is assumed zero over time since the wave-induced motion in heave oscillates about the sea surface. Hence, the following can be stated:

$$p_I^n = \lim_{T\to\infty} \frac{1}{T} \int_0^T p_z^n(t)\mathrm{d}t = 0.$$

   For a in-depth study of the VVR concept, Bryne et al. [21] can be advised.
3. Angular velocity measurements in the $\{b\}$ frame from a three-axis rate gyro with biases: $\boldsymbol{\omega}_{\text{IMU}}^b = \boldsymbol{\omega}_{b/n}^b + \boldsymbol{b}_g^b$. The biases, $\boldsymbol{b}_g^b$, are assumed constant with respect to the system dynamics of (5).
4. Specific forces measurements in the $\{b\}$ frame: $\boldsymbol{f}_{\text{IMU}}^b = \boldsymbol{f}^b$. We assume the accelerometer measurements are bias compensated e.g. as in Grip et al. [22, Sec. VI].
5. Heading measurements from the triple-redundant compass package, $\psi_{\text{c}} = \psi$.

3. OBSERVER DESIGN AND ADAPTIVE-WAVE FILTERING

The objective of the wave-filtering design is to construct LF estimates of position, velocity and heading from the sensor measurements available. The objective is carried out with a modular observer design as seen in Figure 3. First, two feedback-interconnected observers, $\Sigma_1 - \Sigma_2$ are utilized to estimate the vessels position, attitude, linear velocity and gyro bias. These two observers constitutes the strapdown INS. Furthermore, the LF estimates are constructed utilizing the estimates from $\Sigma_1 - \Sigma_2$ and the time-varying encounter frequency, $\omega_e(t)$ provided by a wave-frequency estimator.

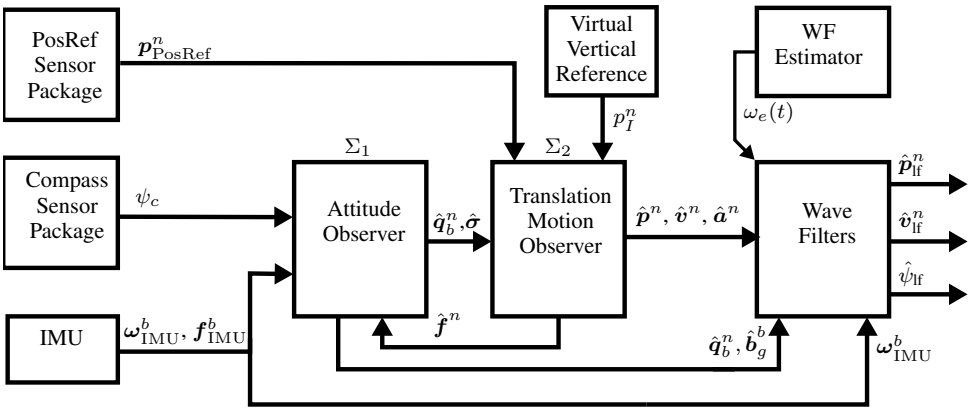

Figure 3. The observers $\Sigma_1 - \Sigma_2$ are aided by triple-redundant compass and position reference sensor packages and a virtual-altitude measurement. The outputs of $\Sigma_1 - \Sigma_2$ together with the encounter frequency $\omega_e(t)$ are provided to the wave-filtering block. The outputs of the wave-filtering block are the LF estimate $\boldsymbol{p}_{\text{lf}}^n$, $\boldsymbol{v}_{\text{lf}}^n$ and ψ_{lf}.

3.1. Estimating the Total Vessel Motion and the Gyro Bias

The total vessel motion is estimated with two feedback-interconnected observers. The first observer, denoted Σ_1, is the attitude observer, represented by the unit quaternion, $\boldsymbol{q}_b^n$, between the {b} and {n} frame and the gyro bias, $\boldsymbol{b}_g^b$, in the {b} frame. The second observer, Σ_2, estimates the translation motion consisting of the specific force, the linear velocity and the position in the $\{n\}$ frame by exploiting the attitude estimate. In addition, the estimate of the specific force, $\hat{\boldsymbol{f}}^n$, is fed back from the translation motion observer, Σ_2, to aid the attitude observer, as seen in Figure 3. This is important since $\boldsymbol{f}^n \neq -\boldsymbol{g}^n$ due to wave excitation of the vessel.

Copyright © 2015 John Wiley & Sons, Ltd.
Prepared using acsauth.cls

DOI: 10.1002/10.1002/acs

The attitude observer, Σ_1, by Grip et al. [22], developed from [23], is given as

$$\Sigma_1 : \begin{cases} \dot{\hat{\boldsymbol{q}}}_b^n = \boldsymbol{T}(\hat{\boldsymbol{q}}_b^n)(\boldsymbol{\omega}_{b/n,\text{IMU}}^b - \hat{\boldsymbol{b}}_g^b + \hat{\boldsymbol{\sigma}}) & (14a) \\ \dot{\hat{\boldsymbol{b}}}_g^b = \text{Proj}\big(\hat{\boldsymbol{b}}_g^b, -k_I(t)\hat{\boldsymbol{\sigma}}\big), & (14b) \end{cases}$$

with the injection term

$$\hat{\boldsymbol{\sigma}} = k_1(t)\boldsymbol{c}^b \times \boldsymbol{R}(\hat{\boldsymbol{q}})^\intercal \boldsymbol{c}^n + k_2(t)\boldsymbol{f}_{\text{IMU}}^b \times \boldsymbol{R}(\hat{\boldsymbol{q}})^\intercal \hat{\boldsymbol{f}}^n \tag{15}$$

where $k_I(t) > 0$ in (14b) and the gains in (15) satisfies $k_1(t) \geq k_P$ and $k_2(t) \geq k_P$ for some $k_P > 0$. The vector measurement based on ψ_c, from the heading reference sensor package, is defined as $\boldsymbol{c}^b := [\cos(\psi_c), -\sin(\psi_c), 0]^\intercal$ whereas the reference vector is defined as $\boldsymbol{c}^n := [1, 0, 0]^\intercal$. $\boldsymbol{f}^b = \boldsymbol{f}_{\text{IMU}}^b$ is measured specific force provided by the accelerometer, while $\hat{\boldsymbol{f}}^n$ is provided by Σ_2 and is the estimated specific force in the {n} frame. Proj$(\cdot,\cdot)$ denotes the parameter projection, from [24, App. E], such that the gyro bias estimate is confined to a compact set, $\|\hat{\boldsymbol{b}}_g^b\| \leq M_g$, as with the previous results presented by Grip et al. [22], [25], [16] and [26].

The translational motion observer, Σ_2, by Bryne et al. [15] is given as:

$$\Sigma_2 : \begin{cases} \dot{\hat{p}}_I^n = \hat{p}_z^n + \vartheta(t)\theta K_{p_I p_I}\tilde{p}_I & (16a) \\ \dot{\hat{\boldsymbol{p}}}^n = \hat{\boldsymbol{v}}^n + \vartheta(t)\theta^2 \begin{bmatrix} \boldsymbol{0}_{2\times 1} \\ K_{pp_I} \end{bmatrix} \tilde{p}_I + \vartheta(t)\theta \boldsymbol{C}_{\text{PosRef}} \boldsymbol{K}_{pp}\tilde{\boldsymbol{p}} & (16b) \\ \dot{\hat{\boldsymbol{v}}}^n = \hat{\boldsymbol{f}}^n + \boldsymbol{g}^n + \vartheta(t)\theta^3 \begin{bmatrix} \boldsymbol{0}_{2\times 1} \\ K_{vp_I} \end{bmatrix} \tilde{p}_I + \vartheta(t)\theta^2 \boldsymbol{C}_{\text{PosRef}} \boldsymbol{K}_{vp}\tilde{\boldsymbol{p}} & (16c) \\ \dot{\boldsymbol{\xi}} = -\boldsymbol{R}(\hat{\boldsymbol{q}}_b^n)\boldsymbol{S}(\hat{\boldsymbol{\sigma}})\boldsymbol{f}_{\text{IMU}}^b + \vartheta(t)\theta^4 \begin{bmatrix} \boldsymbol{0}_{2\times 1} \\ K_{\xi p_I} \end{bmatrix} \tilde{p}_I + \vartheta(t)\theta^3 \boldsymbol{C}_{\text{PosRef}} \boldsymbol{K}_{\xi p}\tilde{\boldsymbol{p}} & (16d) \\ \hat{\boldsymbol{f}}^n = \boldsymbol{R}(\hat{\boldsymbol{q}}_b^n)\boldsymbol{f}_{\text{IMU}}^b + \boldsymbol{\xi}. & (16e) \end{cases}$$

where $\hat{\boldsymbol{p}}^n$ and $\hat{\boldsymbol{v}}^n$ are the estimates of position and linear velocity, respectively in {n}, capturing both the LF and WF motion components of the vessel. $\hat{p}_I^n$ is the estimated integrated heave of the vessel. Moreover, $\boldsymbol{\xi}$ is an intermediate state providing information of the translation motion in the calculation of $\hat{\boldsymbol{f}}^n$. In addition, $\hat{\boldsymbol{a}}^n = \hat{\boldsymbol{f}}^n + \boldsymbol{g}^n$ is the estimated linear acceleration in {n}. This signal is utilized in the wave-filtering scheme as seen in Figure 3 and Section 3.3. $K_{p_I p_I}$, K_{pp_I}, K_{vp_I} and $K_{\xi p_I}$ are scalar gains associated with the integrated heave position and the innovation signal $\tilde{p}_I$, while $\boldsymbol{K}_{pp}$, $\boldsymbol{K}_{vp}$ and $\boldsymbol{K}_{\xi p}$ are gain matrices associated with the position and the innovation signal $\tilde{\boldsymbol{p}}$. Furthermore, $\boldsymbol{C}_{\text{PosRef}}$ is given as

$$\boldsymbol{C}_{\text{PosRef}} = \begin{bmatrix} 1 & 0 & 0 \\ 0 & 1 & 0 \\ 0 & 0 & 0 \end{bmatrix} \text{ or } \boldsymbol{C}_{\text{PosRef}} = \boldsymbol{I}_3$$

where the first prevents the vertical position measurement to be utilized as aid if this component has low precision compared to the horizontal position reference component as with satellites based reference systems. In addition, $\vartheta(t)$ is a scalar time-varying gain, required to fulfill $\vartheta(t) \geq \tau > 0$. Finally, $\theta \geq 1$ is a high-gain tuning parameter used to guarantee stability. $\vartheta(t)$ can be utilized to tune the observer online based on e.g position reference quality indicators such as calculated or reported sensor variance.

The respective estimation errors of the translational motion are defined in the following manner; $\tilde{p}_I := p_I^n - \hat{p}_I^n$, $\tilde{\boldsymbol{p}} := \boldsymbol{p}^n - \hat{\boldsymbol{p}}^n$, $\tilde{\boldsymbol{v}} := \boldsymbol{v}^n - \hat{\boldsymbol{v}}^n$ and $\tilde{\boldsymbol{f}} := \boldsymbol{f}^n - \hat{\boldsymbol{f}}^n$. The attitude and gyro bias estimation error are defined as $\tilde{\boldsymbol{q}} := \boldsymbol{q}_b^n \otimes \hat{\boldsymbol{q}}_b^{n*}$ and $\tilde{\boldsymbol{b}} := \boldsymbol{b}_g^b - \hat{\boldsymbol{b}}_g^b$, respectively. The constraint of the unit quaternion yield zero estimation error when $\tilde{s} = 1$ or equivalently $\|\tilde{\boldsymbol{r}}\| = 0$. Hence, $\tilde{s} = 0$ corresponds to the maximum attitude error of 180° about some axis. Let the estimation errors of $\Sigma_1 - \Sigma_2$ be defined as $\tilde{\boldsymbol{\chi}} := [\tilde{\boldsymbol{r}}^\intercal, \tilde{\boldsymbol{b}}^\intercal]^\intercal$ and $\tilde{\boldsymbol{x}} := [\tilde{p}_I, \tilde{\boldsymbol{p}}^\intercal, \tilde{\boldsymbol{v}}^\intercal, \tilde{\boldsymbol{f}}^\intercal]^\intercal$, respectively. Then, the stability properties of $\Sigma_1 - \Sigma_2$ are given by:

Copyright © 2015 John Wiley & Sons, Ltd.
Prepared using acsauth.cls

DOI: 10.1002/10.1002/acs

Proposition 1 (USGES INS for Marine Craft)
The equilibrium point $[\tilde{\boldsymbol{\chi}}^\intercal,\ \tilde{\boldsymbol{x}}^\intercal]^\intercal = \mathbf{0}$ of the error dynamics of the interconnected system $\Sigma_1 - \Sigma_2$ is USGES.

Proof, see Bryne et al. [15].

3.2. Wave Encounter Frequency

The time-varying encounter frequency, $\omega_e(t)$, is obtained using an the adaptive signal-based algorithm, for instance the GES stable estimator of Belleter et al. [19],

$$\dot{\zeta}_1 = \zeta_2 \tag{17}$$

$$\dot{\zeta}_2 = -\omega_f \zeta_2 - \omega_f^2 \zeta_1 + \omega_f^2 y \tag{18}$$

$$\dot{\hat{\varphi}} = k(t)\zeta_1(\dot{\zeta}_2 - \hat{\varphi}\zeta_1) \tag{19}$$

where y is the input signal, ω_f is the embedded low pass filter's cut-off frequency, $k(t)$ is a positive, smooth time-varying gain and $\varphi = -\hat{\omega}_e(t)^2$ such that $\hat{\omega}(t)$ converges to $\omega(t)$ exponentially fast. By using the pitch estimate, $\hat{\theta}$, provided by $\hat{\boldsymbol{q}}_b^n$ from Σ_1, as the driving input signal such that $y = \hat{\theta}$ result in a cascaded structure where both components have exponential stability properties.

3.3. Adaptive Wave Filtering

This section presents the wave filtering of the INS estimates such that the LF motions are reconstructed from the available signals. The wave-filtering strategy is based on adaptive notch filtering and a time-varying observer design utilizing the model structure from Section 2.3, the time-varying encounter frequency, $\omega_e(t)$, obtained from (17)–(19) and the estimates provided by $\Sigma_1 - \Sigma_2$. With respect to the model (7)–(9), the estimates from $\Sigma_1 - \Sigma_2$ are utilized both as input and measurements in the wave-filtering-observer design as illustrated in Figure 4. Reconstructing the LF signals employing observers, together with notch filters, has the potential to yield less phase-shift compared to utilization of pure notch filters. In addition, the WF components can also be estimated when employing observers. Pure filtering strategies do not have this capability.

Five time-varying observers are proposed to reconstruct the LF motion for horizontal positions, horizontal linear velocities and heading, as indicated in Figure 4. The observers are structurally similar and given by:

$$\dot{\hat{\boldsymbol{x}}}_i = \boldsymbol{A}(t)\hat{\boldsymbol{x}}_i + \boldsymbol{B}u_i + \boldsymbol{K}_i(t)\tilde{y}_i, \quad \tilde{y}_i = y_i - \boldsymbol{C}\hat{\boldsymbol{x}}_i \tag{20}$$

where $\hat{\boldsymbol{x}} = [\hat{\xi}_{\text{wf}},\ \hat{y}_{\text{wf}},\ \hat{y}_{\text{lf}}]^\intercal$. The matrices $\boldsymbol{A}(t)$, $\boldsymbol{B}$ and $\boldsymbol{C}$ are given in (13). The term $\boldsymbol{E}_i w_i$ in (13) is neglected in the design since the observers are solely driven by the innovation signal $\tilde{y}_i$ and the given $\omega(t)$ at time $t \geq t_0$. The LF input u_i is obtained by notch filtering the given signal r_i obtained

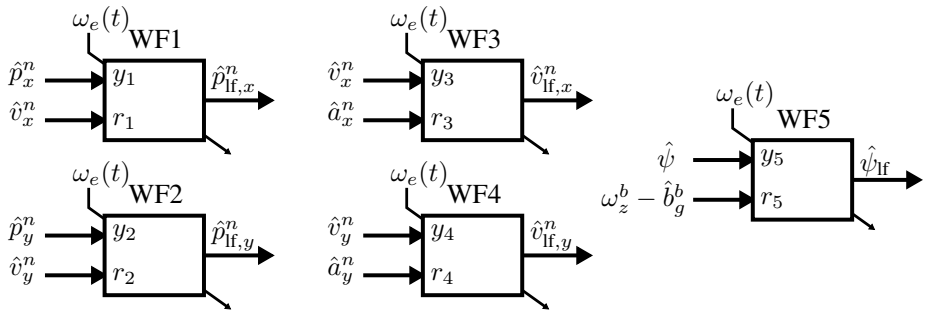

Figure 4. The wave filtering is performed with five time-varying observers. For each signal to be wave filtered is the full-motion estimate utilized as the observer measurement and the corresponding derivative, estimate or measurement, utilized as input to the observer.

Copyright © 2015 John Wiley & Sons, Ltd.
Prepared using acsauth.cls

DOI: 10.1002/10.1002/acs

Table I. Input r_i and output y_i of the wave-filtering observers.

Observer Number	**Measurement** y_i	**Input** r_i
1	$\hat{p}_x^n$	$\hat{v}_x^n$
2	$\hat{p}_y^n$	$\hat{v}_y^n$
3	$\hat{v}_x^n$	$\hat{a}_x^n$
4	$\hat{v}_y^n$	$\hat{a}_y^n$
5	$\hat{\psi}$	$\omega_z^b - \hat{b}_g^b$

from $\Sigma_1 - \Sigma_2$, as:

$$u_i = h_{n_i}(s) r_i, \tag{21}$$

with

$$h_{n_i}(s) = \frac{s^2 + 2\zeta_{n_i}\omega_n s + \omega_n^2}{(s+\omega_n)^2}. \tag{22}$$

The overview of the given input r_i and outputs y_i is presented in Table I. In order to allow for the notch filter to be adaptive, (21)–(22) is realized in state-space form as

$$\dot{\boldsymbol{x}}_{n_i} = \boldsymbol{A}_n(t)\boldsymbol{x}_{n_i} + \boldsymbol{B}_n r_i \tag{23}$$

$$u_i = \boldsymbol{C}_{n_i}(t)\boldsymbol{x}_{n_i} + D_n r_i \tag{24}$$

where

$$\begin{aligned} \boldsymbol{A}_n(t) &= \begin{bmatrix} -2\omega_n(t) & -\omega_n^2(t) \\ 1 & 0 \end{bmatrix}, \boldsymbol{B}_n = \begin{bmatrix} 1 \\ 0 \end{bmatrix}, \\ \boldsymbol{C}_{n_i}(t) &= \begin{bmatrix} 2(\zeta_{n_i} - 1)\omega_n(t) & 0 \end{bmatrix}, \; D_n = 1. \end{aligned} \tag{25}$$

with constant ζ_{n_i}. Then, by choosing $\omega_n(t) = \omega_e(t)$ yields an adaptive notch filtering of the signal input r_i.

The observer gains are given as $\boldsymbol{K}_i(t) = \boldsymbol{P}_i(t)\boldsymbol{C}^\intercal$ where $\boldsymbol{P}_i = \boldsymbol{P}_i^\intercal > 0$ is the positive-definite solution of

$$\dot{\boldsymbol{P}}_i(t) = \boldsymbol{A}(t)\boldsymbol{P}_i(t) + \boldsymbol{P}_i(t)\boldsymbol{A}^\intercal(t) + \boldsymbol{Q}_i(t) \tag{26}$$

with $\boldsymbol{Q}_i(t) = \boldsymbol{Q}_i^\intercal(t) > 0$ as the positive-definite matrix utilized as tuning parameter. The corresponding observer error dynamics is:

$$\dot{\tilde{\boldsymbol{x}}}_i = (\boldsymbol{A}(t) - \boldsymbol{K}_i(t)\boldsymbol{C})\tilde{\boldsymbol{x}}_i. \tag{27}$$

If $\boldsymbol{Q}_i(t)$, $\boldsymbol{A}(t)$ and $\boldsymbol{B}$ are uniformly bounded and the pair $\{\boldsymbol{A}(t), \boldsymbol{C}\}$ is uniformly completely (UCO) observable, entails that $\boldsymbol{P}_i(t)$ will uniformly bounded, that is $c_1\boldsymbol{I}_3 \leq \boldsymbol{P}_i(t) \leq c_2\boldsymbol{I}_3$ for all $t \geq 0$ where $c_1, c_2 > 0$ are two constants (Anderson [27, Lemma 3.2]). Furthermore, this will render the origin of (27) to be GES. $\boldsymbol{A}(t)$ and $\boldsymbol{B}$ are naturally bounded from the model definition of (7)–(9) due to the physical properties of $\omega_e(t)$ and that λ can be chosen as a positive constant. In addition, $\boldsymbol{Q}_i(t)$ is always chosen to be bounded. The following intermediate result insures the uniform completely observability (UCO) properties:

Lemma 1 (UCO of the pair $\{\boldsymbol{A}(t), \boldsymbol{C}\}$)
Assume that λ and $\omega_e(t)$ are positive and uniformly bounded. Then, the pair $\{\boldsymbol{A}(t), \boldsymbol{C}\}$ is UCO.

Proof, see Appendix A.

Uniform boundlessness of $\boldsymbol{P}_i(t)$ follows since $\{\boldsymbol{A}(t), \boldsymbol{C}\}$ is UCO. Hence, the error dynamics (27) is GES.

Copyright © 2015 John Wiley & Sons, Ltd.
Prepared using acsauth.cls

DOI: 10.1002/10.1002/acs

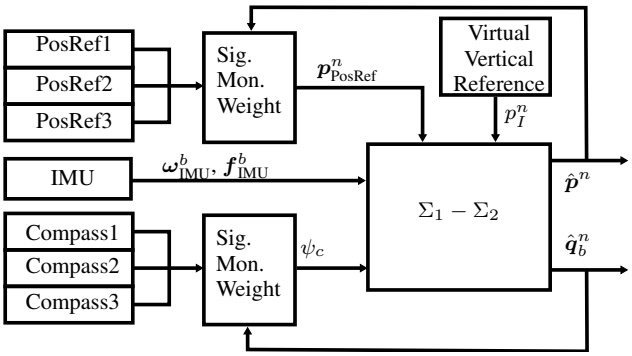

Figure 5. Structure of the triple-redundant signal processing. The sensor voting and sensor weighting takes place in the two respective *Sig. Mon. Weight* blocks. The output of both blocks is utilized by $\Sigma_1 - \Sigma_2$ to estimated the position, $\hat{\boldsymbol{p}}^n$ and the attitude, $\hat{\boldsymbol{q}}^n_b$. Furthermore, the prediction of these signal between sampling are utilized by the sensor-monitoring algorithms. After passing the monitoring test, the weighted measurements $\boldsymbol{p}^n_{\text{PosRef}}$ and ψ_c are utilized by $\Sigma_1 - \Sigma_2$ as aiding measurements.

Remark 1
The gain of the observer (20) is calculated similar to using the continuous Riccati equation of the Kalman-Bucy filter [28]. However, since the given measurement y_i is an smooth estimate form $\Sigma_1 - \Sigma_2$ rather than a sensor reading with additive Gaussian-white noise, the measurement covariance, is omitted from the observer design. Then eq. (23) of Anderson [27] takes the form of $\dot{V}_i = -\tilde{y}_i \boldsymbol{C}_i^{\intercal} \boldsymbol{C} \tilde{y}_i - \tilde{\boldsymbol{x}}^{\intercal} \boldsymbol{P}_i^{-1}(t) \boldsymbol{Q}_i(t) \boldsymbol{P}_i^{-1}(t) \tilde{\boldsymbol{x}} < 0$. Since $\dot{V}$ remains uniformly negative, the results of Anderson also apply for (26)–(27).

4. TRIPLE-REDUNDANT SIGNAL PROCESSING

In order to ensure that the INS and the wave filters have acceptable performance and are fault tolerant, sensor monitoring and sensor weighting should be performed. The respective measurements from the triple-redundant-sensor packages are monitored and processed as illustrated in Figure 5. The signal processing consist of two main components; Signal monitoring and signal weighting. However, first we present the modeling of sensor noise which our design is based upon.

4.1. Sensor Error Modeling and Sensor Faults

The paper will focus on detecting and isolating three type of errors and faults for a single sensor utilizing the structural properties of the triple-redundant-sensor packages together with a high-bandwidth strapdown INS. The typical errors and faults in question are:

- Outliers.
- Fixed bias.
- Drift.

Detection of such errors can be nontrivial due to the dynamics of the PosRefs' measurement errors. Related to position, systems based on dGNSS are the most common reference applied in DP. Therefore we will base our rational on this PosRef system. The transient behavior of the dGNSS-measurement error closely resembles a Gauss-Markov process, as stated by Mohleji and Wang [29, p. 5], due correlation of the dGNSS observation errors in time. In discrete-time this noise model is given by:

$$e_i(k+1) = a(k) e_i(k) + w_i(k), \tag{28}$$

where $w_i(k)$ is the driving Gaussian white noise of the i^{th} measurement and $a(k)$ is the transition parameter

$$a(k) = \exp\left(-\frac{1}{T} T_s\right), \tag{29}$$

Copyright © 2015 John Wiley & Sons, Ltd.
Prepared using acsauth.cls

DOI: 10.1002/10.1002/acs

where T is the time constant and T_s is the sensor sampling interval. For GNSS systems, with differential correction the time constant usually lie between 4-8 minutes as suggested in [29]. The same transient behavior can also be assumed for other DP PosRefs such as hydroacoustic positioning reference systems. The same goes for the gyrocompass which is the nominal heading reference in DP due to class notations such as DVN GL [30].

4.2. Sensor Monitoring and Voting based upon Fault Detection, Isolation and Identification

The fault detection and isolation together with partial diagnosis are performed by modeling the respective faults in discrete-time and exploiting the information available form the redundant sensor packages in a stochastic estimation setup without taking in account the vessel motions.

First the sensor information is modified by utilizing the available information from the INS. A given fault-free measurement $y_i(k)$, at time k, contains information on the craft's motion in addition to the noise of (28) for each respective sensor. In order to analyze the sensor readings for faults separately form the motion of the vessel, the predicted signals from $\Sigma_1 - \Sigma_2$ are utilized to remove the craft's motion components from the respective measurement at each sampling time k. Since the INS provides estimates at significantly higher rate than the respective aiding sensors do, the vessel-motion components can be removed by subtracting the INS prediction $\bar{y}_i$, at time k from the measurement $y(k)$ such as:

$$z_i(k) = y_i(k) - \bar{y}_i, \tag{30}$$

where $\bar{y}_i$ is the INS's last available prediction of y_i before time k. Now, ideally z_i contains sensor noise and faults, i.e $z_i(k) = e_i(k) + f_i(k)$, since the estimates from $\Sigma_1 - \Sigma_2$ are smooth and based on dead reckoning (DR) from IMU data between each of the samples from the respective sensor packages.

The dynamics of transformed measurements $z_i(k), z_i(k+1), \ldots, z_i(k+m)$ can modeled, for each i^{th} sensor reading, in discrete time as:

$$\boldsymbol{x}(k+1) = \boldsymbol{\Phi}(k)\boldsymbol{x}(k) + \begin{bmatrix} w(k) \\ 0 \\ 0 \end{bmatrix} + u(k-\tau_f) \begin{bmatrix} 0 \\ f_b \\ f_r \end{bmatrix} \tag{31}$$

$$z(k) = \boldsymbol{H}(k)\boldsymbol{x}(k) + e(k) \tag{32}$$

similar to Gustafsson [31, p. 296] with

$$\boldsymbol{\Phi}(k) = \begin{bmatrix} a(k) & 0 & 0 \\ 0 & 1 & 1 \\ 0 & 0 & 1 \end{bmatrix}, \quad \boldsymbol{H}(k) = \begin{bmatrix} 1 & 1 & 0 \end{bmatrix}, \tag{33}$$

where the subscript i is omitted for simplicity. Furthermore, $a(k)$ is given by (29) and $w(k)$ is the driving noise of (28). $e(k)$ is the presumed to be Gaussian white measurement noise, while $u(k-\tau_f)$ is the step function

$$u(k-\tau_f) = \begin{cases} 1 & \text{for } k < \tau_f \\ 0 & \text{else} \end{cases}. \tag{34}$$

Moreover, f_b is the sensor bias or drift and f_r is the rate of the bias/drift. Hence, f_r is zero for a fixed bias and is a constant for a drift with constant rate. Then, a sample is deemed fault free if f_b and f_r is contained to a neighborhood around zero. All this implies that $x_1(k)$ corresponds to the sensor noise, while $x_2(k)$ and $x_3(k)$ is the given sensor bias/drift and drift rate, respectively. The system (31)-(32) is observable for $0 < a(k) < 1$ which can be verified with the Kalman-rank-condition test.

Copyright © 2015 John Wiley & Sons, Ltd.
Prepared using acsauth.cls

DOI: 10.1002/10.1002/acs

The senor monitoring is conducted by running a discrete-time Kalman filter with the measurement update

$$\boldsymbol{S}(k) = \boldsymbol{H}(k)\bar{\boldsymbol{P}}(k)\boldsymbol{H}(k) + r(k) \tag{35}$$

$$\boldsymbol{K}(k) = \bar{\boldsymbol{P}}(k)\boldsymbol{C}(k)^{\intercal}\boldsymbol{S}(k)^{-1} \tag{36}$$

$$\hat{\boldsymbol{x}}(k) = \bar{\boldsymbol{x}}(k) + \boldsymbol{K}(k)(z(k) - \boldsymbol{H}(k)\bar{\boldsymbol{x}}(k) \tag{37}$$

$$\begin{aligned}\hat{\boldsymbol{P}}(k) = (\boldsymbol{I} - \boldsymbol{K}(k)\boldsymbol{H}(k))\bar{\boldsymbol{P}}(k)(\boldsymbol{I} - \boldsymbol{K}(k)\boldsymbol{H}(k))^{\intercal} \\ + \boldsymbol{K}(k)r(k)\boldsymbol{K}(k)^{\intercal},\ \hat{\boldsymbol{P}}(k) = \hat{\boldsymbol{P}}^{\intercal}(k) > 0\end{aligned} \tag{38}$$

and the time update

$$\bar{\boldsymbol{x}}(k+1) = \boldsymbol{\Phi}(k)\hat{\boldsymbol{x}}(k) \tag{39}$$

$$\bar{\boldsymbol{P}}(k+1) = \boldsymbol{\Phi}(k)\hat{\boldsymbol{P}}(k)\boldsymbol{\Phi}^{\intercal}(k) + \boldsymbol{\Gamma}(k)\bar{\boldsymbol{Q}}(k)\boldsymbol{\Gamma}^{\intercal}(k), \tag{40}$$

respectively. Even though $w(k)$ only enters the upper state, the process noise of the filter $\boldsymbol{w}(k)$ is chosen $\boldsymbol{w}(k) = [w(k), w_b(k), w_r(k)]^{\intercal}$ such that the estimation scheme is able to identify biased and drifting measurements from measurement sample $k-1$ to k by not considering the fault model to be perfect. In addition, $r = E[e^2(k)]$ is the reported covariance of the sensor noise and $\boldsymbol{Q}(k) = E[\boldsymbol{w}(k)\boldsymbol{w}(k)^{\intercal}]$ is the covariance of the process noise. This again leads to the modified process noise covariance matrix $\bar{\boldsymbol{Q}}(k)$ which can be given by:

$$\bar{\boldsymbol{Q}}(k) = \boldsymbol{Q}(k) - \frac{1}{r}\boldsymbol{M}(k)\boldsymbol{M}(k)^{\intercal} \tag{41}$$

motivated by

$$\mathrm{E}\left[\begin{bmatrix}\boldsymbol{w}^{\intercal}(k)\ v(k)\end{bmatrix}\begin{bmatrix}\boldsymbol{w}(k)\\ e(k)\end{bmatrix}\right] = \begin{bmatrix}\boldsymbol{Q}(k) & \boldsymbol{M}(k)\\ \boldsymbol{M}^{\intercal}(k) & r(k)\end{bmatrix}, \tag{42}$$

as given in Gustafsson [32, Sec. 7.2.3], taking in account the cross correlation between the process noise, $\boldsymbol{w}(k)$ and measurement noise $v(k)$ with respect to the model (28) and the measurement (30). In this case, $\boldsymbol{M}(k) = [m(k), 0, 0]^{\intercal}$ is the cross covariance of the measurement and process noise, where $m(k)$ can be calculated offline as:

$$m(k) = \frac{1}{n-1}\sum_{l=k-n-1}^{k-1}\big(w(l) - \mu_w\big)\big(e(l) - \mu_e\big), \tag{43}$$

and stored in a look-up table where n is the length of a window based on fault-free data. μ_w and μ_e are the receptive means over the same window. The choice of $a(k)$, in $\boldsymbol{\Phi}(k)$, $w(k-n-1), \ldots, w(k-1)$ and $e(k-n-1), \ldots, e(k-1)$ can be calculated prior to the operation based upon previous data collected from the sensor in question. Moreover, this offline analysis should take in account the possibility of changing sensor precision over time. Hence, the look-up table containing $\bar{\boldsymbol{Q}}$ should be based upon process noise data $w(k-n-1), \ldots, w(k-1)$ and measurement noise data $e(k-n-1), \ldots, e(k-1)$ corresponding to a variety sensor covariances $r(k-n-1), \ldots, r(k-1)$ and $a(k)$ such that the $m(k-n-1), \ldots, m(k-1)$ data are valid for changing sensor precision.

Sensor Outlier Detection:
Outlier detection can then be performed with innovation monitoring of the KF (35)–(40) with

$$T(k) = \big(z(k) - \boldsymbol{H}(k)\bar{\boldsymbol{x}}(k)\big)^{\intercal}\boldsymbol{S}^{-1}(k)\big(z(k) - \boldsymbol{H}(k)\bar{\boldsymbol{x}}(k)\big) \tag{44}$$

as in Gustaffson [32, eq. (7.71)]. If $T(k)$ is exceeds a predefined threshold, $z(k)$ is deemed to be an outlier.

Copyright © 2015 John Wiley & Sons, Ltd.
Prepared using acsauth.cls

DOI: 10.1002/10.1002/acs

Sensor Bias and Sensor Drift Detection:
Sudden changes in the mean of $z(k)$ will be detectable with (44) yielding $T(k)$ to spike. The same effect will present it self if the sensor recovers. Then, monitoring of $\hat{\boldsymbol{x}}_2(k)/\bar{\boldsymbol{x}}_2(k)$ should be done in parallel with outlier detection to detect a sensor bias.

Sensor drift is in general the most difficult fault to detect and identify since it not necessarily noticeable in the innovation monitoring of (44) due to a possible low drift rate, f_r. For the same reason, by only monitoring $\hat{\boldsymbol{x}}_3(k)/\bar{\boldsymbol{x}}_3(k)$, the state associated with the drift rate, can be insufficient to detect sensor drift since the rate may be lower the than the process noise of the filter (35)-(39). Therefore, drift detection is performed by monitoring the estimate/prediction $\hat{\boldsymbol{x}}_2(k)/\bar{\boldsymbol{x}}_2(k)$, associated with the sensor bias. Then, sensor drift is detected if the sensor bias estimate surpasses a given threshold regardless of the result from the innovation monitoring. The fault estimation ensures that partial fault diagnosis is obtained.

By following the methodology above instead of typical a voting strategy enables the possibility to detected an erroneous sensor also when only two PosRefs are available. This is due to the IMU measurements are provided at significantly higher rates than the PosRef and compass measurements. This again, allows for $z_i(k)$ to be generated and performing the fault estimation with (35)–(39). However, with only two position and heading references available, this strategy will only work for faster emerging errors. For slowly drifting position reference measurement, an alternative algorithm is presented by Rogne et al. [33]. An other framework for detecting similar faults based on particle filtering is presented by Zhao and Skjetne [34].

4.3. Sensor Weighting

The second step of the redundant-signal processing is measurement weighting. If the given measurement was deemed healthy by the fault-detection algorithms of Section 4.2, the measurements should be weighted. By assuming that sensors have independent noise components, the weighted measurement, $\boldsymbol{x}_w$, of dimension p from N sensors can be obtained from e.g. Gustafsson [32, Ch. 2.2] by minimizing the object function

$$V^{LS} = \sum_{k=1}^{N} \big(\boldsymbol{y}(k) - \boldsymbol{H}(k)\boldsymbol{x}_w(k)\big)^{\intercal} \boldsymbol{R}^{-1}(k) \big(\boldsymbol{y}(k) - \boldsymbol{H}(k)\boldsymbol{x}_w(k)\big). \tag{45}$$

where $\boldsymbol{y}(k) \in \mathbb{R}^{p \cdot N}$ is the vector of measurements at time k. $\boldsymbol{x}_w(k) \in \mathbb{R}^p$ represents the weighted measurement while $\boldsymbol{H}_w(k) = \big[I_{p_1}, \ldots, I_{p_N}\big]^{\intercal}$ yielding,

$$\boldsymbol{x}_w(k) = \boldsymbol{R}_w(k)\boldsymbol{H}_w^{\intercal}(k)\boldsymbol{R}^{-1}(k)\boldsymbol{y}(k). \tag{46}$$

Here $\boldsymbol{R}(k)$ is a block-diagonal matrix of the reported covariance matrices from the respective sensors. In this paper, these covariances are $E[e_{c_i}^2(k)]$ and $E[\boldsymbol{e}_{\mathrm{PosRef},i}(k)\, \boldsymbol{e}_{\mathrm{PosRef},i}(k)^{\intercal}]$ with respect to the possible sensor components of (32). Then, $\boldsymbol{x}_w$ is the weighted measurement, in a least squares sense with covariance $\boldsymbol{R}_w(k) = \big(\boldsymbol{H}_w(k)^{\intercal}\boldsymbol{R}^{-1}(k)\boldsymbol{H}_w(k)\big)^{-1}$, and utilized in the INS measurement updates.

Remark 2
The assumption of independent sensor noise is not true for PosRefs such as satellite based navigation and for hydroacoustic position reference (HPR) systems. This is due to the noise being time correlated for dGNSS receivers within the same geographical area and for each pair of HPR transponders and transducers. In DP, differential correction regarding GNSS is applied to reduce common-mode errors, however there are still some residual common-mode errors present after the correction. Nevertheless, this assumption have still be proven to be useful in Kalman filter based observer designs with position measurements from such position references.

Copyright © 2015 John Wiley & Sons, Ltd.
Prepared using acsauth.cls

DOI: 10.1002/10.1002/acs

5. CASE STUDY

5.1. Implementation

The sensor measurements were generated using the Marine Systems Simulator [35] simulating a offshore supply vessel employing a DP system. The vessel's wave-induced motions were generated by exposing the vessel to wave forces and moments generated with the JONSWAP wave spectra. The significant wave height and peak frequency were chosen to $H_s = 7$ meters and $\omega = 0.8$ [rad/s], respectively. The IMU and the respective observers where simulated at 100 Hz. The chosen heading and position reference were three gyrocompasses and three dGNSS, simulated at 10 Hz and 1 Hz, respectively.

All the sensors were simulated with noise. The dGNSS and gyrocompasses noise were simulated with a first-order Gauss-Markov process of (28), where Table II present parameters related to the transient noise for the respective sensor packages. When the compasses were not sampled, the injection term of Σ_1 was implemented as

$$\hat{\boldsymbol{\sigma}} = k_2(t)\boldsymbol{f}^b_{\text{IMU}} \times \boldsymbol{R}(\hat{\boldsymbol{q}})^\intercal \hat{\boldsymbol{f}}^n. \tag{47}$$

Because of the slow dynamics of DP vessels, this will not affect the performance of Σ_1 even though the stability analyses of Bryne et al. [15] and the reference therein requires two vector measurements. The quaternion unity constraint was enforced with $\hat{\boldsymbol{q}}^n_b = \hat{\boldsymbol{q}}^n_b / \|\hat{\boldsymbol{q}}^n_b\|$ after every quaternion update. Σ_2 was implemented with the discrete-time corrector-predictor scheme presented in Fossen [1, Ch. 11.3.4] such that the dGNSS measurement update of Σ_2 was carried out every 100th IMU sample.

The implementation of time-varying wave filters were carried out with exact discretization at 100 Hz. The design parameter ζ_{n_i} of (23)–(25) was chosen $\zeta_{n_i} = 0.05$ for all five adaptive notch filters.

5.2. Tuning and Gain Structure

The gains of Σ_1 was tuned with $g_a = [k_1(t),\, k_2(t),\, k_I(t)]^\intercal$, and

$$\dot{g}_a = -\frac{1}{T} g_a + \frac{1}{T} k_a, \begin{cases} k_a = [20,\, 20,\, 1]^\intercal & \text{if } t \leq 100 \\ k_a = [0.55,\, 0.55,\, 0.01]^\intercal & \text{else.} \end{cases}$$

with $T = 25$ s to speed up the initial convergence of the $\hat{\boldsymbol{q}}^n_b$ and $\hat{\boldsymbol{b}}^b_g$. This is similar to [15] such that unnecessary amplification of sensor noise is avoided when the attitude estimates have converged. The fixed gains of Σ_2, on compact form,

$$\boldsymbol{K}_t = \begin{bmatrix} K_{p_I p_I} & \boldsymbol{0}_{1\times 2} & K_{p_z p_I} & \boldsymbol{0}_{1\times 2} & K_{v_z p_I} & \boldsymbol{0}_{1\times 2} & K_{\xi_z p_I} \\ \boldsymbol{0}_{2\times 1} & \bar{\boldsymbol{K}}^\intercal_{pp} & \boldsymbol{0}_{2\times 1} & \bar{\boldsymbol{K}}^\intercal_{vp} & \boldsymbol{0}_{2\times 1} & \bar{\boldsymbol{K}}^\intercal_{\xi p} & \boldsymbol{0}_{2\times 1} \end{bmatrix}^\intercal,$$

with $\bar{\boldsymbol{K}}_{pp} = \boldsymbol{T}\boldsymbol{K}_{pp}\boldsymbol{T}^\intercal$, $\bar{\boldsymbol{K}}_{vp} = \boldsymbol{T}\boldsymbol{K}_{vp}\boldsymbol{T}^\intercal$, $\bar{\boldsymbol{K}}_{\xi p} = \boldsymbol{T}\boldsymbol{K}_{\xi p}\boldsymbol{T}^\intercal$ and $\boldsymbol{T} = [1, 0, 0; 0, 1, 0]$ were calculated as $\boldsymbol{K}_t = \boldsymbol{P}_t\boldsymbol{C}_t^\intercal$ where $\boldsymbol{P}_t$ is the solution of

$$\boldsymbol{A}_t\boldsymbol{P}_t + \boldsymbol{P}_t\boldsymbol{A}_t^\intercal + \boldsymbol{Q}_t - 2\tau\boldsymbol{P}_t\boldsymbol{C}_t^\intercal\boldsymbol{C}_t\boldsymbol{P}_t = \boldsymbol{0} \tag{48}$$

Table II. Parameters of dGNSS and gyrocompass error model.

Parameter	**dGNSS (hor. comp.)**	**Compass**
Time Constant	$T = 240$ [s]	$T = 60$ [s]
Std. $v(k)$	1.10 [m]	0.14 [°]
Std $w(k)$	0.1 [m]	0.025 [°]
Covariance $w(k), v(k)$	0.01 [m]	-
Std. $v(k)$ (low precision)	2.17 [m]	-
Std $w(k)$ (low precision)	0.2 [m]	-
Covariance $w(k), v(k)$ (low precision)	0.04 [m]	-

Copyright © 2015 John Wiley & Sons, Ltd.
Prepared using acsauth.cls

DOI: 10.1002/10.1002/acs

Table III. PosRef and gyro compass validity threshold

Thresholds	PosRef (north and east comp.)	Compass
Outlier	8 [m]	4 [°]
Bias/drift	2 [m]	1.2 [°]

where $\boldsymbol{A}_t$ and $\boldsymbol{C}_t$ is given in [15, Eq. (11)]. The numerical values of $\boldsymbol{Q}_t$ and τ were chosen as:

$$\boldsymbol{Q}_t = 1 \cdot 10^{-3}\text{diag}\{2.5 \cdot 10^{-3}, 1, 1, 2.5 \cdot 10^{-3}, 1, 1, 2.5 \cdot 10^{-3}, 1, 1, 2.5 \cdot 10^{-3}\}$$

and $\tau = 1/2$ which resulted in $K_{p_I p_I} = 0.5222$, $K_{p_z p_I} = 0.1363$, $K_{v_z p_I} = 0.0208$, $K_{\xi_z p_I} = 0.0016$, $\bar{\boldsymbol{K}}_{pp} = 0.6387 \cdot \boldsymbol{I}_2$, $\bar{\boldsymbol{K}}_{vp} = 0.2035 \cdot \boldsymbol{I}_2$ and $\bar{\boldsymbol{K}}_{\xi p} = 0.0316 \cdot \boldsymbol{I}_2$. Furthermore, the time-varying gain component, $\vartheta(t)$, of Σ_2 was implemented as

$$\dot{\vartheta} = -\frac{1}{T}\vartheta + \frac{1}{T}k_{tv}, \quad k_{tv} = \begin{cases} 0.5 & \text{(low)} \quad \text{if GNSS}_{\text{rms}} > l_{\text{high}} \\ 0.75 & \text{(med)} \quad \text{if GNSS}_{\text{rms}} > l_{\text{low}} \text{ and GNSS}_{\text{rms}} < l_{\text{high}} \\ 1 & \text{(high)} \quad \text{if GNSS}_{\text{rms}} < l_{\text{low}} \text{ or time} < 100 \end{cases} \tag{49}$$

where $\text{GNSS}_{\text{rms}} = (R_{w,\text{xx}}(k) + R_{w,\text{yy}}(k))^{0.5}$ is obtained from the weighting algorithm of (46), such that $\vartheta(t)$ remains smooth even though the gain is modified over time. Furthermore, $l_{\text{low}} = 0.9$ and $l_{\text{high}} = 1.7$ where chosen as the gain thresholds, together with $T = 5$, such that $\vartheta(t)$ will be adaptive with respect to PosRef quality. Moreover, $\theta = 1$ was chosen. The two position wave filters were tuned with $\boldsymbol{Q}_i = \text{diag}(0.01, 2.5^2, 0.5)$, while the velocity and heading wave filters were tuned as $\boldsymbol{Q}_i = \text{diag}(0.01, 2^2, 0.5)$. Finally, different $\bar{\boldsymbol{Q}}_i(k)$ were precalculated for each axis of the dGNSS and the compass measurements. These were based on the parameters of Table II including different $\bar{\boldsymbol{Q}}_i(k)$ for low and high dGNSS variance. Regarding the gyrocompass, $\bar{\boldsymbol{Q}}(k) = \boldsymbol{Q}(k)$ was chosen since the cross correlation between the process noise and the measurement noise was deemed negligible based on the parameters of Table II. The fault-detection thresholds were chosen as presented in Table III.

5.3. Simulation Results

This section presents the simulation results of the combined INS, with wave filtering and the triple-redundant signal processing as presented in Section 3–4. In order to illustrate the effect of the time-varying wave filters and the triple-redundant signal processing the following situations regarding the dGNSS and compass measurements were simulated:

- At time 350 and 400 seconds the position of dGNSS3 spiked with minus five meters north and five meters south.
- Between 400-500 seconds the precision of dGNSS2 was reduced where the standard deviation doubled as described in Section 5.1. In addition, dGNSS2 began to drift 0.1 m/s in the same time period. According to Chen et al. [36], such drift can be due to differential link error.
- Between 450-500 seconds dGNSS3 did not provide any measurements.
- Between 600-700 seconds the quality of all three dGNSS deteriorated as described in Section 5.1, Table II.
- At 800 seconds the third gyrocompass began to lag before recovering when time approached 1000 seconds.
- At 1000 seconds dGNSS reference was lost due to e.g. powerful ionospheric scintillation.

Figure 6 shows the estimated pitch, from Σ_1, feeding the WF estimator together with output of the WF estimator, $\omega_e(t)$. The fast convergence of the pitch estimated, seen in Figure 6a, was due to the time-varying tuning scheme presented in Section 5.2. The estimate of $\omega_e(t)$ began to settle to the wave-encounter frequency after 250 seconds as seen in Figure 6b.

Figure 7 shows the high-performance gyro bias estimate together with the respective estimation error. The z-axis of the gyro bias estimate was further fed to the heading wave filter, as illustrated

Copyright © 2015 John Wiley & Sons, Ltd.
Prepared using acsauth.cls

DOI: 10.1002/10.1002/acs

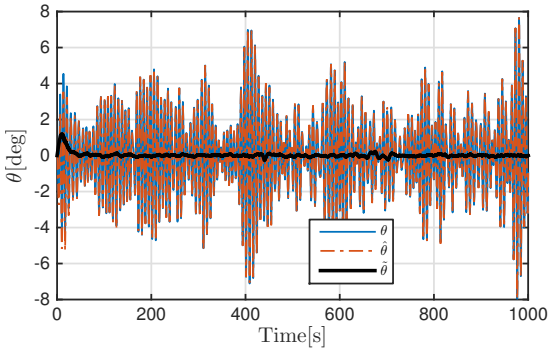

(a) Pitch estimate provided by Σ_1.

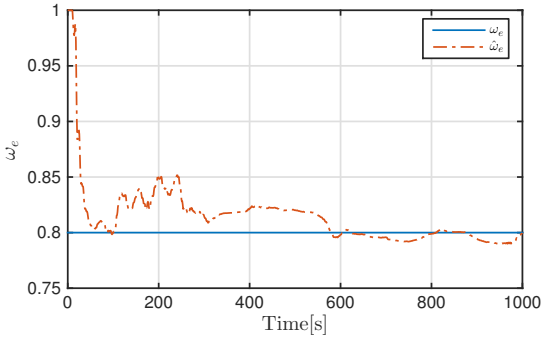

(b) Estimate of ω_e from the WF estimator.

Figure 6. Evolution of the pitch estimate which acts as the driving signal in the estimation of $\omega_e(t)$ together with the wave-encounter frequency provided by (17)–(19).

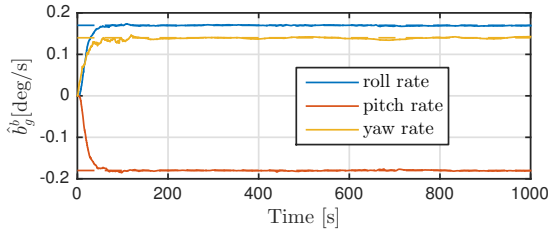

(a) Gyro bias estimate.

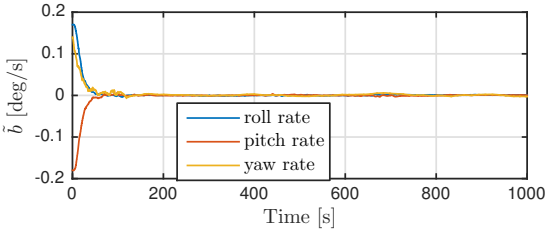

(b) Gyro bias estimation error.

Figure 7. Evolution of the gyro bias estimate, provided by Σ_1.

in Figure 4, to compensate for the gyro bias before the yaw rate measurements entered the heading wave filter. The transient performance of the gyro bias estimates are achieved, as with the pitch estimate, due to the time-varying tuning as presented in Section 5.2.

Figure 8 present the position, velocity, and attitude estimation errors. One can observe that the vertical position and velocity errors are considerably smaller than then horizontal counterparts. This is due to only the VVR measurement was utilized to stabilize the vertical axes. Since the vertical axes are self contained, while the horizontal axes are dependent of dGNSS quality with the respective transient measurement errors, the horizontal estimation errors are bigger then the vertical. From this and the fact that the vertical GNSS measurements are worse than the horizontal counterparts, one can argue that the inclusion of the VVR to the INS is beneficial, compared to vertical aiding from dGNSS. The velocity error is less effected by the transient dGNSS error since the gains, associated with the velocity, are smaller than the position gains as presented in Section 5.2. The transient heading error, in Figure 8c, is due to the gyrocompass measurement error.

In Figure 9, the wave-filtered heading, $\hat{\psi}_{\text{lf}}$, together with the adaptive notch-filtered gyro measurement, r_f is presented. The effect of the heading wave filtering, seen in Figure 9a, is evident where the majority of the WF motion is not present in the LF estimates. The bias-compensated and notch-filtered yaw rate measurements are shown in Figure 9b.

The adaptive notch-filtered acceleration input to the velocity wave filters are shown in Figure 10 together with the estimated acceleration, $\hat{\boldsymbol{a}}^n = \hat{\boldsymbol{f}}^n + \boldsymbol{g}^n$. The effect of the adaptive notch filter is obvious where the filtered acceleration estimates are significantly smoother than the signal which they are based upon.

This leads to the wave filtering of velocity and position. Figure 11 show the LF estimates of position, $\hat{\boldsymbol{p}}^n_{\text{lf}}$, and linear velocity, $\hat{\boldsymbol{v}}^n_{\text{lf}}$, versus both the estimated vessel's position and linear velocity provided by the INS. The transient of the LF estimates seen in the first seconds are due to the encounter frequency estimate has not yet converged. Furthermore, this resulted in the observers of (20) and the notch filters of (23)–(24) were not performing optimally before $\hat{\omega}_e(t)$ converged to

Copyright © 2015 John Wiley & Sons, Ltd.
Prepared using acsauth.cls

DOI: 10.1002/10.1002/acs

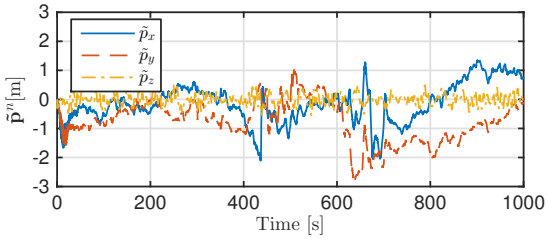

(a) Position estimation error.

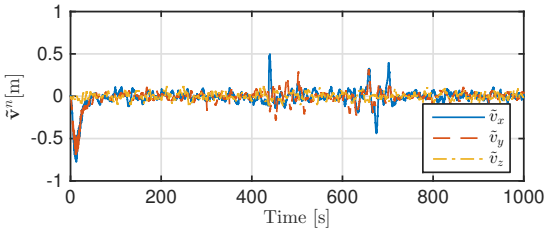

(b) Velocity estimation error.

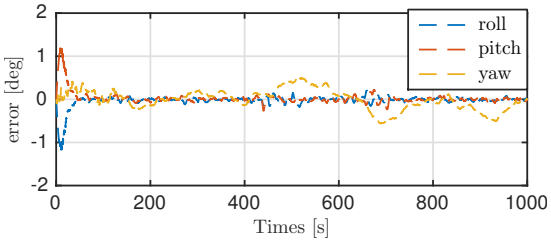

(c) Attitude estimation error

Figure 8. Position, velocity and attitude estimation errors.

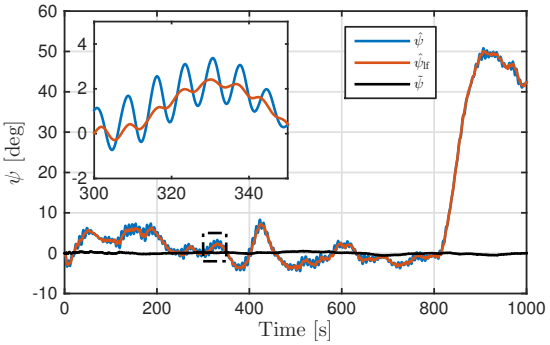

(a) Estimated heading vs estimated LF heading.

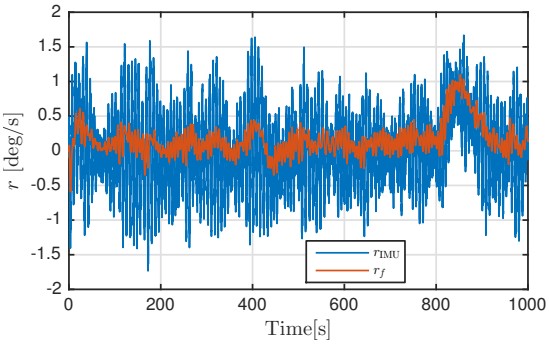

(b) Measured yaw rate (blue) versus filtered yaw rate (red).

Figure 9. The estimated yaw angle from Σ_1 together with the wave-filtered yaw estimate, estimated WF heading motion and gyro bias compensated filtered yaw rate.

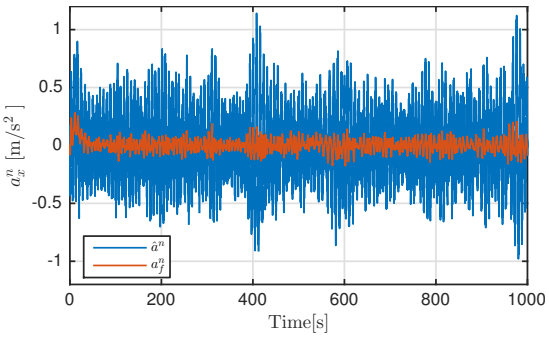

(a) North

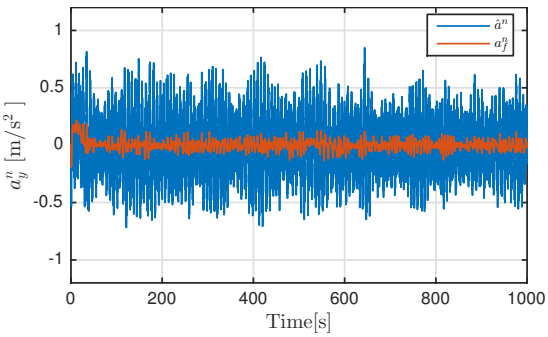

(b) East.

Figure 10. Estimated and filtered estimated acceleration $\boldsymbol{a}^n = \boldsymbol{f}^n + \boldsymbol{g}^n$ in North and East where the filtered estimates enter the linear velocity wave filters. Blue: Estimated. Red: Filtered.

$\omega_e(t)$. After the transients settled, one can clearly observe that the wave filters reconstructed the LF positions and velocities adequately.

Copyright © 2015 John Wiley & Sons, Ltd.
Prepared using acsauth.cls

DOI: 10.1002/10.1002/acs

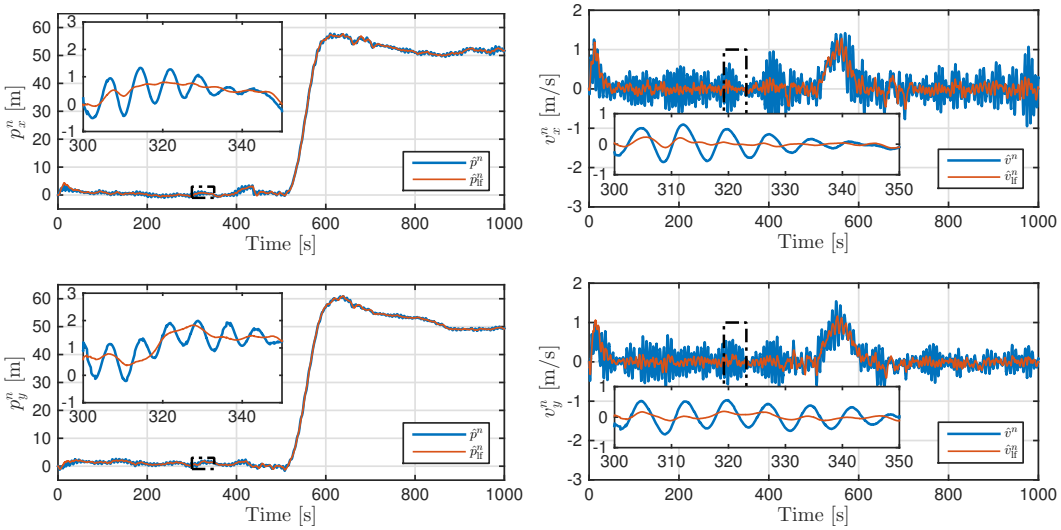

(a) LF position estimates versus the estimated position provided by Σ_2.

(b) LF velocity estimates versus the estimated velocity provided by Σ_2.

Figure 11. LF position and LF velocity estimates versus the estimates provided by the INS.

Results regarding the dGNSS sensor package, related to signal monitoring and weighting can be seen in Figures 12–13. In Figure 12a one can observe that the measurements from dGNSS3 at time 300 seconds and at 350 seconds are outliers. Furthermore, from Figure 12b one notices that measurements from GNSS2 slowly drifts between 400 and 500 seconds. The outliers of GNSS3 and the drift of dGNSS2 were detected with the innovation monitoring and bias/drift detection, respectively. This is indicated by Figure 12d, showing how the status of the respective dGNSS receivers evolved with the faults described above. The results of the dGNSS wild-point detection is seen in Figure 12c, while the drift estimation of dGNSS2 is seen in Figures 12e–12f, respectively. dGNSS2 was rejected when the drift estimate surpassed the bias/drift thresholds level of Table III. In addition, one can observe in Figure 12c that the innovation monitoring spikes multiple times after the measurements from dGNSS2 were rejected. This is due to $\bar{y}_i$ of (30), now only is based on fault-free information since the INS estimates are only aided with non-erroneous dGNSS measurements. Then, $z_i[k]$ will have an offset compared to $\bar{y}_i$ since $y_i[k]$, related to dGNSS2 drifts. This again verifies that it was correct to dismiss the measurements from dGNSS2 in the given time period. In addition, the rejection of dGNSS2 and dGNSS3, seen in Figure 12d at approximate 650 and 700 seconds, respectively were due to the bias monitoring incorrectly estimated biases/drift at these instances in time due to the transient error dGNSS measurement surpassed the bias/drift threshold.

Figure 13 shows the weighted dGNSS measurements and the weighed covariance, The former is almost unaffected by the simulated errors as seen in Figure 13. The resulting effects of the sensor monitoring related to the weighted dGNSS covariance can be seen in Figure 13b. An increase is seen when dGNSS2 and dGNSS3 were rejected. Furthermore, it can be seen that the weighted covariance increases at 450 seconds since dGNSS3 fails to provide measurements. At approximately 500 seconds both dGNSS2 and dGNSS3 recovered, as seen in Figure 12d, such that the weighted-dGNSS covariance decreased. Figure 13b also shows an increase in the weighted dGNSS covariance in the time frame of 600 to 700 seconds, however, with larger magnitude than before. This is due to the increase of noise in the measurements provided by all three receivers. In addition, Figure 13b also shows the evolution of the time-varying gain $\vartheta(t)$ based on the weighted covariance provided by the dGNSS triple-redundant sensor packages. One can observe that ϑ decreases when the weighted covariance increases and vice versa.

Figure 14 illustrates signal monitoring and weighting of the triple-redundant gyrocompass sensor package. Figure 14a shows how the third gyrocompass begins to lag after 800 seconds, while the weighted measurements in Figure 14d are unaffected by the this fault. This is due to the sensor

Copyright © 2015 John Wiley & Sons, Ltd.
Prepared using acsauth.cls

DOI: 10.1002/10.1002/acs

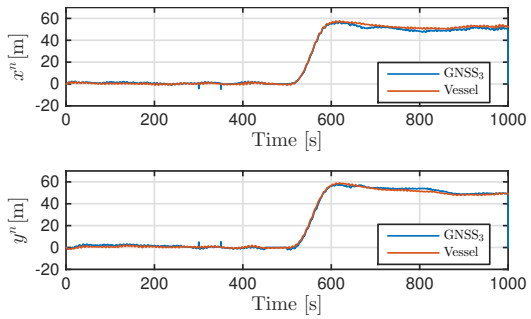

(a) Position measurements from dGNSS3 versus the vessel's position. Outliers are observed at 350 and 400 seconds.

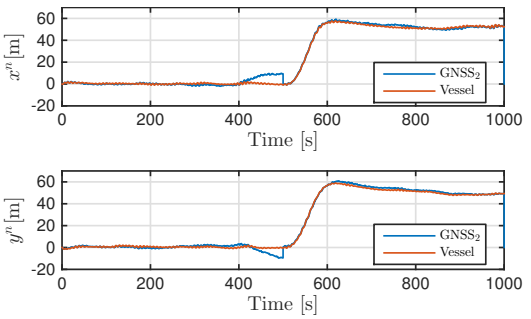

(b) Positions measurements from dGNSS2 versus the vessel's positions. dGNSS2 drifts between 400 and 500 seconds.

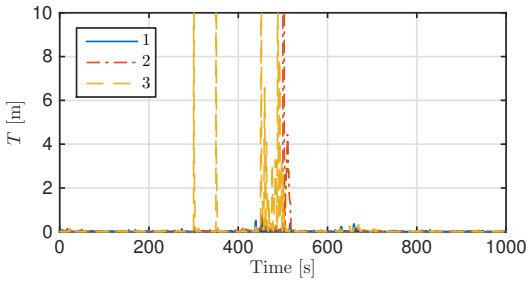

(c) Outlier monitoring of east components of the dGNSS sensor package

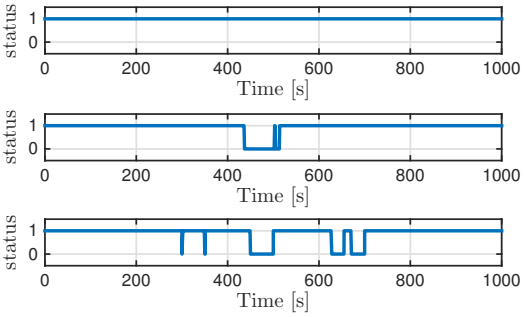

(d) GNSS status. Accepted and rejected measurements are represented by 1 and 0, respectively.

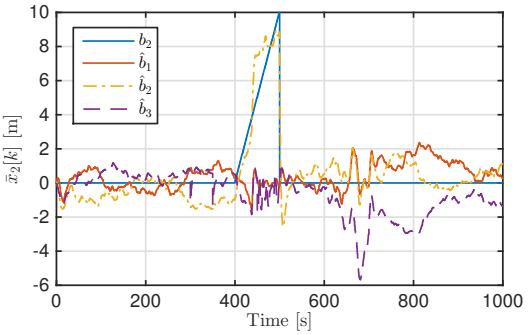

(e) Estimates of the bias/drift of the north dGNSS measurement component.

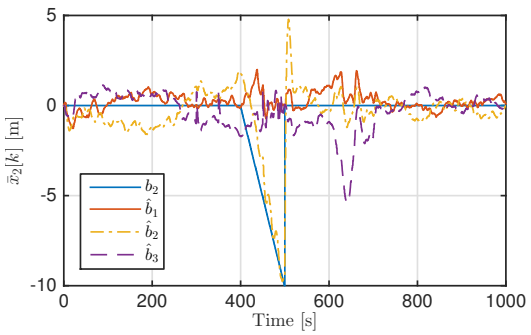

(f) Estimates of the bias/drift of the east dGNSS measurement component

Figure 12. dGNSS faults and fault monitoring. dGNSS2 provided erroneous measurements between 400-500 seconds of simulation, while the dGNSS3 measurements spiked at 350 and 400 seconds of simulation. All of the GNSS measurements becomes less accurate between 600-700 seconds of simulation.

monitoring excludes the third gyrocompass approximately 30 seconds after the compass fails to capture the change in heading, as seen in Figure 14c, since the bias/drift estimate surpassed the threshold of Table III. The bias/drift estimates related to the compass measurements are presented in Figure 14b. In addition, one can see that compass1 was rejected at approximately 200 and 280 seconds and the compass3 was rejected at approximately 150 seconds. These are falsely-detected compass errors induced by the low-threshold value in Table III and the transient measurements error of the compasses at the given instances in time.

Figure 15 show results related to GNSS loss. Figure 15a displays the drift of the LF position estimates relative the actual ship's position. This is reasonable since the INS, which the LF estimates are based upon, will drift when the aiding sensor is lost. In Figure 15b one can see that the heading estimates are unaffected by this. This is due to three factors. First, the heading estimate is mainly

Copyright © 2015 John Wiley & Sons, Ltd.
Prepared using acsauth.cls

DOI: 10.1002/10.1002/acs

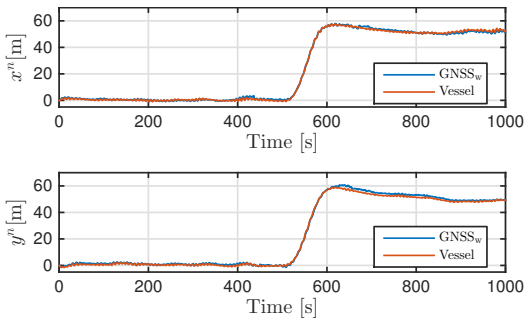

(a) Weighted position measurements from the dGNSS sensor package versus the vessel's positions

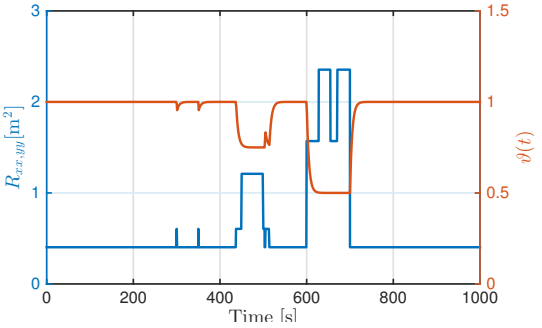

(b) Covariance of the weighted dGNSS measurements versus the time-varying gain $\vartheta(t)$.

Figure 13. Results of the dGNSS sensor weighting.

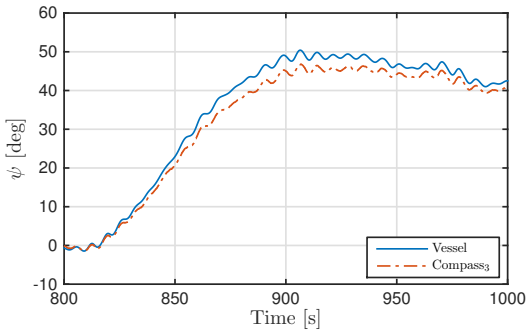

(a) The lagging heading measurements from the third gyrocompass versus the vessel's heading.

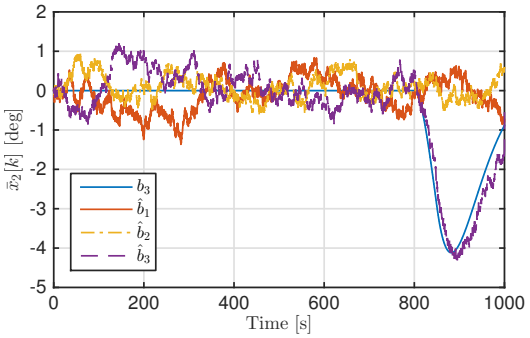

(b) Compass bias/drift estimates.

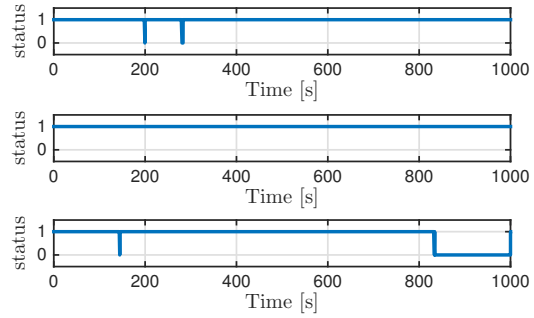

(c) Compass sensor status. Accepted and rejected measurements are represented by 1 and 0, respectively.

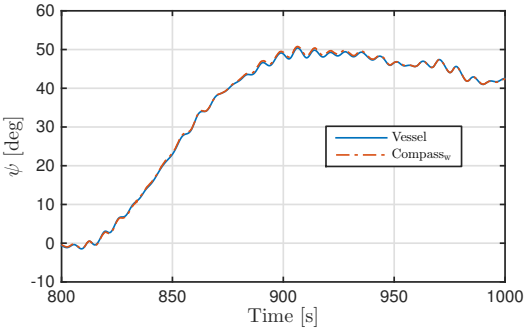

(d) Weighted measurements from the gyrocompass-sensor package versus the vessel's heading.

Figure 14. Results of the triple-redundant signal possessing of the heading sensor package where compass3 provided lagging measurements after 800 seconds of simulation

based on the compass measurements, secondly, the $\boldsymbol{\xi}$ term in $\hat{\boldsymbol{f}}^n$, from Σ_2, will in general be small after $\Sigma_1 - \Sigma_2$ have converged. This makes the attitude observer robust to loss of position references for shorter time periods. This statement is supported by Figure 15c. The third factor is that the gyro bias is still estimated with high accuracy, as seen in Figure 15d. An other possible reason for the attitude estimation performance persists, is that the vertical axis of Σ_2 is stabilized independently of position reference with the VVR. Because of this, the kinematic coupling between heave and roll/pitch, together with wave excitation, probably also contribute to the adequate performance of Σ_1 even though the feedback from the horizontal position is lost.

Copyright © 2015 John Wiley & Sons, Ltd.
Prepared using acsauth.cls

DOI: 10.1002/10.1002/acs

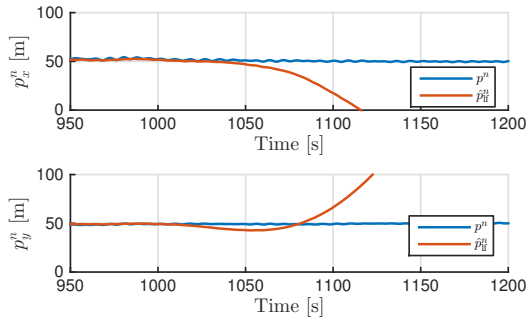

(a) Drifting LF position estimates (red). Vessel position (blue)

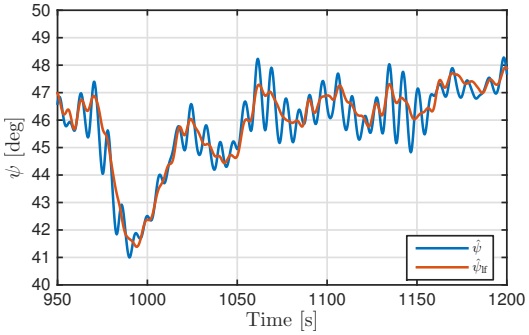

(b) Heading estimates (blue) and LF heading estimates (red)

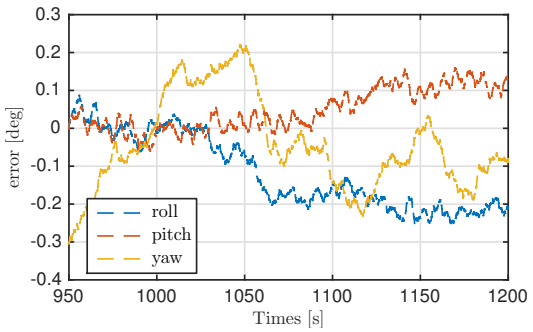

(c) Attitude estimation error

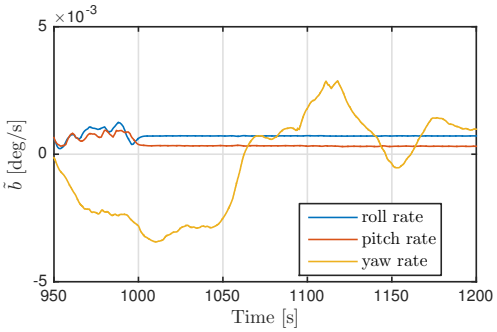

(d) Gyro bias estimation error

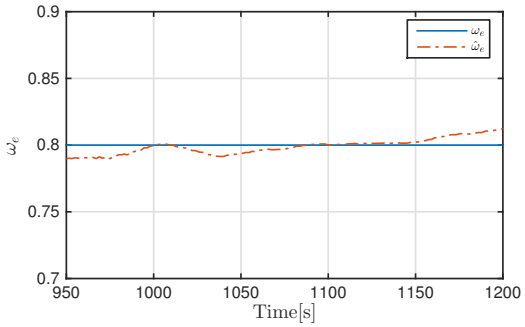

(e) Wave-encounter frequency (blue). Wave-encounter frequency estimates (red).

Figure 15. Effects of loss of position reference at 1000 seconds. Figure 15a shows the drifting LF position estimates, while Figure 15c show the attitude estimation performance, in large extent, is still maintained. Figure 15d shows the gyro bias estimation error remains small. The same goes the estimates of the $\omega_e(t)$ (Figure 15e). The LF heading estimates are seen in Figure 15b relative the estimated heading from Σ_1.

6. CONCLUDING REMARKS

A marine vessel wave-filtering strategy for INS aided by triple-redundant position and heading reference systems have been presented. This includes two observers with exponential stability properties, designed with Lyapunov stability theory. The additional wave filtering is performed with five time-varying GES observers separating the low-frequency and wave-frequency motion components of position, linear velocities and heading estimates, respectively obtained from the INS. The wave filtering is adaptive with respect to the time-varying wave encounter frequency. Furthermore, triple-redundant sensor monitoring and weighting were performed to monitor the sensor packages, employing the possibility to exclude faulty measurements.

Copyright © 2015 John Wiley & Sons, Ltd.
Prepared using acsauth.cls

DOI: 10.1002/10.1002/acs

Simulations show how the time-varying wave-filtering strategy successfully generates low-frequency estimates from the noisy measurements. In addition, the IMU based triple-redundant-sensor monitoring and weighting scheme, proposed in this paper, proved to be successful in detecting and estimating realistic sensor errors. Also fault tolerance related to position reference loss is achieved since heading was maintained independent of position.

A. PROOF OF LEMMA 1

Since $\boldsymbol{A}(t)$ is time-varying, the rank condition for observability does not directly apply. Observability for time-varying system can, among others, be obtained through calculating the observability co-distribution applying Lie derivatives $L_0, L_1, \ldots, L_{n-1}$ for a system of dimension n. See, e.g. Nijmeijer and Schaft [37, Ch. 3.1] for details.

Theorem 3.32 of Nijmeijer and Schaft [37, Ch. 3.1] entails that the pair $\{\boldsymbol{A}(t), \boldsymbol{C}\}$ is uniformly observable if and only if the observability co-distribution, $\mathrm{d}\mathcal{O}$ has full rank, e.i

$$\operatorname{rank}(\mathrm{d}\mathcal{O}) = n \tag{50}$$

for all $t \geq 0$.

The observability co-distribution takes the form of

$$\mathrm{d}\mathcal{O} = \begin{bmatrix} L_0(t) \\ L_1(t) \\ L_2(t) \end{bmatrix} = \begin{bmatrix} \boldsymbol{C} \\ \boldsymbol{C}\boldsymbol{A}(t) \\ \boldsymbol{C}\boldsymbol{A}^2(t) + \boldsymbol{C}\dot{\boldsymbol{A}}(t) \end{bmatrix} \tag{51}$$

$$= \begin{bmatrix} 0 & 1 & 1 \\ -\omega_e^2(t) & -2\lambda\omega_e(t) & 0 \\ 2\lambda\omega_e^3(t) - 2\omega_e(t)\dot{\omega}_e(t) & 4\lambda^2\omega_e^2(t) - 2\omega_e(t) - 2\lambda & 0 \end{bmatrix}. \tag{52}$$

Suppose that, at an instance in time, $\dot{\omega}_e(t) = \lambda\omega_e^2(t)$ such that

$$\mathrm{d}\mathcal{O} = \begin{bmatrix} 0 & 1 & 1 \\ -\omega_e^2(t) & -2\lambda\omega_e(t) & 0 \\ 0 & 4\lambda^2\omega_e^2(t) - 2\omega_e(t) - 2\lambda & 0 \end{bmatrix}. \tag{53}$$

By investigation of the null space of $\mathrm{d}\mathcal{O}$, i.e. $\mathrm{d}\mathcal{O}\boldsymbol{x} = 0$, where $\boldsymbol{x}$ is the state vector, yields

$$x_2 + x_3 = 0 \tag{54}$$

$$-\omega_e^2(t)x_1 - 2\lambda\omega_e(t)x_2 = 0 \tag{55}$$

$$\big(4\lambda^2\omega_e^2(t) - 2\omega_e(t) - 2\lambda\big)x_2 = 0. \tag{56}$$

resulting in

$$\begin{aligned} &\text{eq. (56) implies: } x_2 = 0, \\ &\text{eq. (54) implies: } x_3 = -x_2 = 0, \\ &\text{eq. (55) implies: } x_1 = \frac{2\lambda}{\omega_e^2(t)}x_2 = 0 \end{aligned}$$

from the properties of $0 < \omega_{e,\min} \leq \omega_e(t) \leq \omega_{e,\max} < \infty$, and that $\lambda > 0$ is a constant. Now suppose that $\dot{\omega}_e(t) = 0$. Then,

$$\mathrm{d}\mathcal{O} = \begin{bmatrix} 0 & 1 & 1 \\ -\omega_e^2(t) & -2\lambda\omega_e(t) & 0 \\ 2\lambda\omega_e^3(t) & 4\lambda^2\omega_e^2(t) - 2\omega_e(t) - 2\lambda & 0 \end{bmatrix}. \tag{57}$$

Copyright © 2015 John Wiley & Sons, Ltd.

Prepared using acsauth.cls
DOI: 10.1002/10.1002/acs

Again, by investigation of the null space, $\mathrm{d}\mathcal{O}\boldsymbol{x} = 0$, results in

$$x_2 + x_3 = 0 \tag{58}$$

$$-\omega_e^2(t)x_1 - 2\lambda\omega_e(t)x_2 = 0 \tag{59}$$

$$2\lambda\omega_e^3(t)x_1 + \big(4\lambda^2\omega_e^2(t) - 2\omega_e(t) - 2\lambda\big)x_2 = 0. \tag{60}$$

The validity of (59)–(60) hold if and only if $x_1 = x_2 = 0$ which implies that (58) can only be zero for $x_3 = -x_2 = 0$. Then, since $\boldsymbol{C}$ is constant, $\omega_e(t)$ is positive and uniformly bounded and λ is a positive constant, $\mathrm{d}\mathcal{O}$ cannot take any other form than presented in (53) and (57). Hence, the pair $\{\boldsymbol{A}(t), \boldsymbol{C}\}$ is uniformly observable for all $t \geq 0$ since

$$\dim \mathrm{null}(\mathrm{d}\mathcal{O}) = 0 \Rightarrow \mathrm{rank}(\mathrm{d}\mathcal{O}) = 3, \forall t \geq 0,$$

for all constellations of $\mathrm{d}\mathcal{O}$. □

ACKNOWLEDGEMENT

This work has been carried out at the Centre for Autonomous Marine Operations and Systems (AMOS) and supported by the The Research Council of Norway and Rolls-Royce Marine. The Research Council of Norway is acknowledged as the main sponsor of AMOS.

References

1. Fossen TI. *Handbook of Marine Craft Hydrodynamics and Motion Control*. John Wiley & Sons, Ltd., 2011.
2. Balchen J, Jenssen NA, Sælid S. Dynamic positioning using Kalman filtering and optimal control theory. *In the IFAC/IFIP Symposium On Automation in Offshore Oil Field Operation*, Bergen, Norway, 1976; 183—186.
3. Sælid S, Jenssen NA, Balchen JG. Design and analysis of a dynamic positioning system based on the Kalman filtering and optimal control. *IEEE Transactions on Automatic Control* 1983; **28**(3):331 – 339.
4. Fossen TI, Perez T. Kalman filtering for positioning and heading control of ships and offshore rigs. *IEEE Control Systems Magazine* 2009; **29**(6):32–46, doi:10.1109/MCS.2009.934408.
5. Vik B, Fossen TI. Semiglobal exponential output feedback control of ships. *IEEE Transaction On Control System Technology* 1997; **5**(3):360–370, doi:10.1109/87.572132.
6. Lauvdal T, Fossen TI. Robust adaptive ship autopilot with wave filter and integral action. *Special Issue on Marine Systems Control, International Journal of Adaptive Control and Signal Processing* 1998; **12**(8):605–622, doi:10.1002/(SICI)1099-1115(199812)12:8<605::AID-ACS516>3.0.CO;2-1.
7. Fossen TI, Strand JP. Passive nonlinear observer design for ships using lyapunov methods: full-scale experiments with a supply vessel. *Automatica* 1999; **35**(1):3 – 16, doi:10.1016/S0005-1098(98)00121-6.
8. Strand JP, Fossen TI. Nonlinear passive observer design for ships with adaptive wave filtering. *New Directions in Nonlinear Observer Design*, *LNCIS*, vol. 244, Nijmeijer H, Fossen TI (eds.). Springer-Verlag, 1999; 113–134.
9. Torsetnes G, Jouffroy J, Fossen TI. Nonlinear dynamic positioning of ships with gain-scheduled wave filtering. *Proc. IEEE Conference on Decision and Control*, Paradise Island, Bahamas, 2004, doi:10.1109/CDC.2004.1429657.
10. Nguyen TD, Sørensen AJ, Quek ST. Design of hybrid controller for dynamic positioning from calm to extreme sea conditions. *Automatica* 2007; **43**(5):768–785, doi:10.1016/j.automatica.2006.11.017.
11. Brodtkorb AH, Sørensen AJ, Teel A. Increasing the operation window for dynamic positioned vessels using the concept of hybrid control. *Proc. of the ASME 2014 33rd International Conference on Ocean, Offshore and Arctic Engineering, OMAE2014*, San Francisco, California, USA, 2014.
12. Hassani V, Sørensen AJ, Pascoal AM, Aguiar A. Multiple model adaptive wave filtering for dynamic positioning of marine vessels. *Proc. of the American Contr. Conf.*, Fairmont Queen Elizabeth, Montréal, Canada, 2012; 6222–6228, doi:10.1109/ACC.2012.6315094.
13. Hassani V, Pascoal AM, Sørensen AJ. A novel methodology for adaptive wave filtering of marine vessels: Theory and experiments. *Proc. IEEE Conference on Decision and Control*, Florence, Italy, 2013; 6162–6167, doi:10.1109/CDC.2013.6760863.
14. Hassani V, Sørensen AJ, Pascoal AM. Adaptive wave filtering for dynamic positioning of marine vessels using maximum likelihood identification: Theory and experiments. *Proc of the 9th IFAC Conference on Control Applications in Marine Systems*, Osaka, Japan, 2013, doi:10.3182/20130918-4-JP-3022.00041.
15. Bryne TH, Fossen TI, Johansen TA. Nonlinear observer with time-varying gains for inertial navigation aided by satellite reference systems in dynamic positioning. *IEEE Mediterranean Conference on Control and Automation*, Palermo, Italy, 2014; 1353–1360, doi:10.1109/MED.2014.6961564.
16. Grip HF, Fossen TI, Johansen TA, Saberi A. Nonlinear observer for GNSS-aided inertial navigation with quaternion-based attitude estimation. *Proc. of the American Contr. Conf.*, Washington, DC, 2013; 272–279, doi:10.1109/ACC.2013.6579849.

Copyright © 2015 John Wiley & Sons, Ltd.
Prepared using acsauth.cls

17. Lindegaard KP, Fossen TI. A model based wave filter for surface vessels using position, velocity and partial acceleration feedback. *Proc of the 40th IEEE Conference on Decision and Control*, 2001; 946–951, doi:10.1109/.2001.980231.
18. Veksler A, Johansen TA, Skjetne R. Transient power control in dynamic positioning - governor feedforward and dynamic thrust allocation. *Proc. IFAC Conference on Manoeuvring and Control of Marine Craft*, Arenzano, Italy, 2012; 158–163, doi:10.3182/20120919-3-IT-2046.00027.
19. Belleter DJ, Galeazzi R, Fossen TI. Experimental verification of a globally exponentially stable nonlinear wave encounter frequency estimator. *Ocean Engineering, Elsevier* 2015; **97**(15):48–56, doi:10.1016/j.oceaneng.2014.12.030.
20. Godhavn JM. Adaptive tuning of heave filter in motion sensor. *OCEANS '98 Conf. Proc.*, vol. 1, Nice, France, 1998; 174–178, doi:10.1109/OCEANS.1998.725731.
21. Bryne TH, Fossen TI, Johansen TA. A virtual vertical reference concept for GNSS/INS applications at the sea surface. *Proc. IFAC Conference on Manoeuvring and Control of Marine Craft*, Copenhagen, Denmark, 2015.
22. Grip HF, Fossen TI, Johansen TA, Saberi A. Attitude estimation using biased gyro and vector measurements with time-varying reference vectors. *IEEE Trans. Automat. Contr.* 2012; **57**(5):1332—1338, doi:10.1109/TAC.2011.2173415.
23. Mahony R, Hamel T, Pflimlin JM. Nonlinear complementary filters on the special orthogonal group. *IEEE Trans. Automat. Contr.* 2008; **53**(5):1203–2018, doi:10.1109/TAC.2008.923738.
24. Krstić M, Kanellakopoulos I, Kokotović PV. *Nonlinear and Adaptive Control Design*. Wiley: New York, 1995.
25. Grip HF, Fossen TI, Johansen TA, Saberi A. A nonlinear observer for integration of GNSS and IMU measurements with gyro bias estimation. *Proc. of the American Contr. Conf.*, Montreal, Canada, 2012; 4607–4612, doi:10.1109/ACC.2012.6314929.
26. Grip HF, Fossen TI, Johansen TA, Saberi A. Globally exponentially stable attitude and gyro bias estimation with application to GNSS/INS integration. *Automatica* January 2015; **51**:158—166, doi:10.1016/j.automatica.2014.10.076.
27. Anderson B. Stability properties of Kalman-Bucy filters. *Journal of the Franklin Institute* 1971; **1**(2):137–144.
28. Kalman R, Bucy R. New results in linear filtering and prediction theory. *American Society of Mechanical Engineers – Transactions – Journal of Basic Engineering Series D* 1961; **83**(1):95–108.
29. Mohleji SC, Wang G. Modeling ADS-B position and velocity errors for airborne merging and spacing in interval management application. https://www.mitre.org/sites/default/files/pdf/10_3026.pdf, The MITRE Corporation, 7515 Colshire Drive, McLean VA 22102 September 2010.
30. DNV GL. Newbuildings special equipment and systems – additional class. *Rules for classification of ships newbuildings*. Part 6, Chapter 7, , 2011. Updated January 2012.
31. Gustafsson F. *Adaptive filtering and change detection*. John Wiley & Sons, Ltd, 2000.
32. Gustafsson F. *Statistical Sensor Fusion*. 2nd edn., Studentlitteratur, 2012.
33. Rogne RH, Johansen TA, Fossen TI. Observer and IMU-based detection of faults in position reference systems and gyrocompasses with dual redundancy in dynamic positioning. *Proc of the IEEE Conference on Control Applications (CCA)*, Antibes, France, 2014; 83–88, doi:10.1109/CCA.2014.6981333.
34. Zhao B, Skjetne R. A unified framework for fault detection and diagnosis using particle filter. *Modeling, Identification and Control* 2014; **35**(4):303—315, doi:10.4173/mic.2014.4.7.
35. MSS Marine Systems Simulator. Viewed 01.08.2014, www.marinecontrol.org 2010.
36. Chen H, Moan T, Verhoeven H. Effect of dGPS failures on dynamic positioning of mobile drilling units in the North Sea. *Accident Analysis and Prevention* 2009; **41**(6):1164–1171, doi:10.1016/j.aap.2008.06.010.
37. Nijmeijer H, der Schaft AV. *Nonlinear dynamical control systems*. Springer-Verlag, 1990.

Copyright © 2015 John Wiley & Sons, Ltd.
Prepared using acsauth.cls